

MICROCOPY RESOLUTION TEST CHART
NATIONAL BUREAU OF STANDARDS-1963-A

UNCLASSIFIED

SECURITY CLASSIFICATION OF THIS PAGE (When Data Entered)

AD-A185 359
OTIC FILE COPY

REPORT DOCUMENTATION PAGE		READ INSTRUCTIONS BEFORE COMPLETING FORM
1. REPORT NUMBER AFIT/CI/NR 87-59T	2. GOVT ACCESSION NO. A185 359	3. RECIPIENT'S CATALOG NUMBER
4. TITLE (and Subtitle) Fiber-Optic Accelerometer Investigation	5. TYPE OF REPORT & PERIOD COVERED THESIS/DISSERTATION	
	6. PERFORMING ORG. REPORT NUMBER	
7. AUTHOR(s) Waldemar Zukauskas	8. CONTRACT OR GRANT NUMBER(s) ①	
9. PERFORMING ORGANIZATION NAME AND ADDRESS AFIT STUDENT AT: Massachusetts Institute of Technology	10. PROGRAM ELEMENT, PROJECT, TASK AREA & WORK UNIT NUMBERS	
11. CONTROLLING OFFICE NAME AND ADDRESS AFIT/NR WPAFB OH 45433-6583	12. REPORT DATE 1987	
	13. NUMBER OF PAGES 83	
14. MONITORING AGENCY NAME & ADDRESS (if different from Controlling Office)	15. SECURITY CLASS. (of this report) UNCLASSIFIED	
	15a. DECLASSIFICATION/DOWNGRADING SCHEDULE	
16. DISTRIBUTION STATEMENT (of this Report) APPROVED FOR PUBLIC RELEASE; DISTRIBUTION UNLIMITED		
17. DISTRIBUTION STATEMENT (of the abstract entered in Block 20, if different from Report)		
18. SUPPLEMENTARY NOTES APPROVED FOR PUBLIC RELEASE: IAW AFR 190-1		Lynn E. Wolaver 17 Aug 87 Dean for Research and Professional Development AFIT/NR
19. KEY WORDS (Continue on reverse side if necessary and identify by block number)		
20. ABSTRACT (Continue on reverse side if necessary and identify by block number) ATTACHED		DTIC ELECTE S OCT 26 1987 D CD

DD FORM 1473 1 JAN 73 EDITION OF 1 NOV 65 IS OBSOLETE

SECURITY CLASSIFICATION OF THIS PAGE (When Data Entered)

87 10 14 279

Author: Capt Waldemar Zukauskas, USAF

Title: FIBER-OPTIC ACCELEROMETER INVESTIGATION

Date: 1987

Pages: 83

Degree: Master of Science in
Aeronautics and Astronautics

Institution: Massachusetts Institute of Technology

ABSTRACT



A fiber-optic accelerometer concept based on the radial displacement of a hollow cylinder subject to acceleration is experimentally investigated. The accelerometer configuration consists of two PZT cylinders wrapped with 2.3 meters of high birefringent single mode fiber placed in a differential configuration. Cylinder radial displacement induces an axial strain into the fiber which stretches the fiber, causing a simultaneous optical path length and index of refraction change. The result is an overall phase change of the light propagating in the fiber. Acceleration is hence measured by detecting and scaling the phase change. Optical common mode rejection is achieved via a 90 degree fiber rotation and splice. Polarization, phase, and temperature stability for the system with and without optical common moding is investigated. A theoretical system scale factor and bias is calculated and used to determine the minimum detectable acceleration sensed for a 50 volt dc step input simulating induced acceleration. System noise is examined and compared to the photon shot noise limit.

Preliminary results for this system indicate a 21 fold improvement in thermal drift stability of the optical common moded system over the noncommon moded system. Splicing the fiber, as compared to an intact fiber, decreased the polarization stability of the system by an order of magnitude from $10^{-4}/m$ to $10^{-3}/m$. The phase stability remained unchanged at $10^{-2}/m$ prior to and after 90 degree fiber rotation and splicing. The primary noise in the system was phase noise due to acoustic perturbations, vibrations in the optical setup, cleaved fiber end backscatter at the optical common mode rejection splice, and nonexact 90 degree fiber rotation for optical common mode rejection. The acceleration sensed due to the 50 volt dc step input was 2.18 g's for this system with a minimum rms detectable acceleration of .13 g's. Further experimentation is required to reduce the signal noise level to a 10^{-7} theoretical limit and to achieve a possible 4 order of magnitude increase in optical common mode rejection.

59

FIBER-OPTIC ACCELEROMETER
INVESTIGATION

by

Waldemar Zukauskas
Captain, United States Air Force

B.S., United States Air Force Academy
(1980)

SUBMITTED IN PARTIAL FULFILLMENT
OF THE REQUIREMENT FOR THE
DEGREE OF

MASTER OF SCIENCE IN
AERONAUTICS AND ASTRONAUTICS

at the

MASSACHUSETTS INSTITUTE OF TECHNOLOGY

October 1986

© Waldemar Zukauskas, 1986



Accession For	
NTIS CRA&I	<input checked="" type="checkbox"/>
DTIC TAB	<input type="checkbox"/>
Unannounced	<input type="checkbox"/>
Justification	
By	
Distribution/	
Availability Codes	
Dist	Avail and/or Special
A-1	

Signature of Author

Waldemar Zukauskas

Department of Aeronautics and Astronautics
October 1986

Certified by

Raymond Carroll

Raymond Carroll
Technical Advisor

Certified by

Shaoul Ezekiel

Professor Shaoul Ezekiel
Thesis Advisor

Accepted by

Professor Harold Y. Wachman
Chairman, Department Graduate Committee

FIBER-OPTIC ACCELEROMETER

INVESTIGATION

by

Waldemar Zukauskas

Submitted to the Department of Aeronautics and
Astronautics on 9 October 1986 in partial fulfillment of the
requirements for the degree of Master of Science in
Aeronautical and Astronautical Engineering

ABSTRACT

A fiber-optic accelerometer concept based on the radial displacement of a hollow cylinder subject to acceleration is experimentally investigated. The accelerometer configuration consists of two PZT cylinders wrapped with 2.3 meters of high birefringent single mode fiber placed in a differential configuration. Cylinder radial displacement induces an axial strain into the fiber which stretches the fiber, causing a simultaneous optical path length and index of refraction change. The result is an overall phase change of the light propagating in the fiber. Acceleration is hence measured by detecting and scaling the phase change. Optical common mode rejection is achieved via a 90 degree fiber rotation and splice. Polarization, phase, and temperature stability for the system with and without optical common mode is investigated. A theoretical system scale factor and bias is calculated and used to determine the minimum detectable acceleration sensed for a 50 volt dc step input simulating induced acceleration. System noise is examined and compared to the photon shot noise limit.

Preliminary results for this system indicate a 21 fold improvement in thermal drift stability of the optical common moded system over the noncommon moded system. Splicing the fiber, as compared to an intact fiber, decreased the polarization stability of the system by an order of magnitude from $10^{-4}/m$ to $10^{-3}/m$. The phase stability remained unchanged at $10^{-2}/m$ prior to and after 90 degree fiber rotation and splicing. The primary noise in the system was phase noise due to acoustic perturbations, vibrations in the optical setup, cleaved fiber end

backscatter at the optical common mode rejection splice, and nonexact 90 degree fiber rotation for optical common mode rejection. The acceleration sensed due to the 50 volt dc step input was 2.18 g's for this system with a minimum rms detectable acceleration of .13 g's. Further experimentation is required to reduce the signal noise level to a 10^{-7} theoretical limit and to achieve a possible 4 order of magnitude increase in optical common mode rejection.

Thesis Supervisor: Shaoul Ezekiel

Title: Professor of Aeronautics and Astronautics, and
Computer Science

ACKNOWLEDGMENTS

First and foremost, I would like to express my thanks to my wife, Suzette, for her constant support and understanding during my studies at M.I.T. Next, my deepest appreciation goes to all the Department 30P resonator gyro personnel at the Charles Stark Draper Laboratory. Of these I would especially like to thank the following for their contributions: Bruce Porter whose constant guidance and encouragement helped make this experimental work both accomplishable and enjoyable; Todd Kaiser whose laboratory experience and help was invaluable during system reconfigurations and optical setups; Joe Scoppettuolo whose electrical design skills shed light on many trying signal detection/processing problems; Richard Regan and Oldrich Laznicka for the use of critically needed optic and electronic components, and Oldrich's many practical "laboratory" suggestions and help during critical data taking; and also Sean O'Connor and Kevin Champagne for their relentless and timely technical support. Lastly, my thanks go to Dr. Raymond Carroll and Professor Shaoul Ezekiel who made thesis work in the fiber-optics area possible, rewarding, and meaningful.

I hereby assign my copyright of this thesis to the Charles Stark Draper Laboratory, Inc., Cambridge, Massachusetts.


Waldemar Zukauskas

Permission is hereby granted by the Charles Stark Draper Laboratory, Inc., to the Massachusetts Institute of Technology to reproduce any or all of this thesis.

TABLE OF CONTENTS

<u>Chapter</u>		<u>Page</u>
1	INTRODUCTION.....	1
	1.1 Motivation.....	1
	1.2 Thesis Outline.....	3
2	REVIEW OF FIBER-OPTIC ACCELEROMETER SYSTEMS.....	5
	2.1 Introduction.....	5
	2.2 Mistubishi Corp., Photoelastic Effect Fiber-Optic Accelerometer.....	5
	2.3 Tilting-Mirror Fiber-Optic Accelerometer.....	9
	2.4 Solid/Hollow Cylinder Fiber-Optic Accelerometer.....	14
	2.5 CSDL Fiber-Optic Accelerometer Concept.....	16
3	THEORY OF OPERATION OF THE CSDL FIBER-OPTIC ACCELEROMETER CONCEPT.....	19
	3.1 Introduction.....	19
	3.2 Fiber Birefringence and Its Application to the CSDL Fiber-optic Accelerometer Concept.....	19
	3.3 Origin and Types of Birefringence Mechanisms Contributing to the Light Phase Delay in the CSDL Concept.....	21
	3.3.1 Bending Birefringence.....	21
	3.3.2 Tension - Coiling Birefringence.....	23
	3.3.3 Transverse Stress Birefringence.....	24
	3.3.4 Internal Birefringence of a High Birefringent Single-Mode Fiber.....	26

TABLE OF CONTENTS (continued)

<u>Chapter</u>	<u>Page</u>
3.4 AB and AL Contributions to Phase Change in the CSDL Concept.....	29
3.4.1 Linear Combination of Resultant Phase Changes Due to Birefringence Mechanisms for the Tension Coiled Low Birefringent Fiber Case.....	31
3.4.2 Linear Combination of Resultant Phase Changes Due to Birefringence Mechanisms for the Nontension Coiled High Birefringent Fiber Base.....	34
3.5 Drum To Fiber Transduction Equation.....	36
3.5.1 Theoretical Phase Change Prediction for a Nominal Single Aluminum Cylinder Wrapped with Low Birefringence Tension Coiled Fiber...37	37
3.5.2 Theoretical Phase Change Prediction for a Nominal Single PZT Cylinder Nontension Coiled High Birefringence Fiber.....	38
3.6 CSDL Fiber-Optic Accelerometer Concept Incorporating Phase Modulation.....	39
 4 PRELIMINARY EXPERIMENTAL INVESTIGATION OF THE CSDL FIBER-OPTIC ACCELEROMETER CONCEPT.....	 46
4.1 Introduction.....	46
4.2 Tension Coiling a High Birefringent Fiber Around A Cylindrical Drum.....	46
4.3 Experimental Phase Change Determination of a Single Cylinder Wrapped with Low Birefringent Tension Coiled Fiber.....	46

TABLE OF CONTENTS (continued)

<u>Chapter</u>		<u>Page</u>
4.4	Experimental Phase Change Determination of a Single PZT Cylinder Wrapped with High Birefringent Nontension Coiled Fiber.....	51
4.5	Polarization, Phase, and Temperature Stability Without Common Mode Rejection.....	53
4.5.1	Polarization Stability of Each Individual High Birefringent Fiber/PZT Cylinder System...	53
4.5.2	Phase and Temperature Stability of Each Individual High Birefringent Fiber/PZT Cylinder System.....	55
4.5.3	Polarization, Phase, and Temperature Stability of the Two Cylinder High Birefringent System.....	57
4.6	Polarization, Phase, and Temperature Stability With Common Mode Rejection.....	60
4.7	Experimental Demonstration of Acceleration Sensing.....	63
5	EXPERIMENTAL DISCUSSION OF RESULTS.....	65
6	SUMMARY, CONCLUSIONS, AND RECOMMENDATIONS.....	69
6.1	Summary and Conclusions.....	69
6.2	Recommendations.....	70
	REFERENCES.....	73

LIST OF ILLUSTRATIONS

<u>Figure</u>		<u>Page</u>
1	Orthogonal polarization mode propagation in an epoxy resin sample.....	7
2	Mitsubishi Corporation photoelastic effect fiber-optic accelerometer configuration.....	8
3	Tilting-mirror fiber-optic accelerometer sensor structure...	10
4	Tilting-mirror fiber-optic accelerometer functional drawing.....	11
5	Tilting-mirror fiber-optic accelerometer light profile at zero induced acceleration.....	13
6	Solid/hollow cylinder fiber-optic accelerometer configuration.....	15
7	CSDL fiber-optic accelerometer concept with optical common mode rejection.....	17
8	Bending birefringence.....	22
9	Transverse stress birefringence.....	25
10a	Nondifferential phase modulation.....	44
10b	Differential phase modulation.....	44
11	Phase modulation via an external phase modulator.....	45
12	Single cylinder system configuration.....	48
13	Tension coiled low birefringence/aluminum cylinder interference curve.....	50
14	Nontension coiled high birefringence/PZT cylinder case.....	52
15	Single cylinder thermal and phase stability data.....	56
16	Two cylinder thermal and phase stability data.....	58
17	Signal at quadrature for the two cylinder system.....	59
18	Two cylinder system with common mode rejection configuration.....	61
19	Common mode rejection thermal drift data.....	62
20	Common mode rejection V_{π} and induced acceleration data.....	64
21	Frequency controlled loop closure.....	72

CHAPTER 1

INTRODUCTION

1.1 Motivation

With the increased requirement for smaller, less expensive, and more accurate inertial measurement systems by the military and civilian sector (for ballistic missile strapdown inertial guidance systems, upper stage satellite booster navigation and guidance systems, large space structure vibrational sensors, etc.), accelerometers operating over a wide dynamic range under adverse conditions are required. To date, the most sensitive conventional fielded accelerometers can be classified into two categories: 1) pendulous servo-force rebalance accelerometers and 2) vibrating element accelerometers. The pendulous servo-force rebalance type consists of an unbalanced, free-pivoting (jewel bearing, flexural spring, etc.), pendulous mass which becomes displaced angularly with applied acceleration. This angular displacement is sensed by a position detector (usually an inductive type pick-off coil) converted into a proportional ac signal, amplified and fed back to a restoring coil fixed to the pendulum surrounded by a permanent magnetic field. The current travelling to the restoring coil induces a restoring torque equal and opposite to the original torque produced by the induced acceleration. A good example of such a pendulous type system is the CSDL-developed Pendulous Integrating Gyro Accelerometer. Pendulous servo-force rebalance accelerometers are usually very complex and laborious to produce/assemble, require substantial warm-up time, are not easily miniaturized, and are fairly expensive. Their performance is currently at the 10^6 dynamic range, limited primarily by material hysteresis.¹

Vibrating element accelerometers, on the other hand, utilize vibrating wire attached to both ends of a proof mass and the accelerometer casing, to detect acceleration. Here the difference in

vibrational frequencies caused by the wire tension change as the proof mass is linearly displaced due to acceleration is detected and scaled to the induced acceleration. To date, a refined version of this concept is the Vibrating Quartz Crystal Beam Accelerometer, developed and marketed by the Singer Company.² Unlike the vibrating wire, the vibrating beam attached to a flexure supported proof mass responds to tension and compression, and requires no initial bias tension to function -- eliminating a major cause of bias instability. Furthermore, the vibrating beam accelerometer's tension and compression response allows for a push-pull configuration (where two vibrating beams are utilized - one placed in compression, the other in tension, as the system experiences induced acceleration), which helps cancel nonlinear and thermal effects. Compared to the pendulous servo-force rebalance accelerometer, the vibrating quartz crystal beam accelerometer has a dynamic range of 10^7 , limited only by quartz crystal configuration asymmetries, quartz beam/proof mass attachment, and proof mass flexure stability as well as material hysteresis.³

Fiber-optic accelerometers are a new approaching breed of acceleration sensors. These systems vary in approach, but basically have the following in common: they utilize a change in light intensity to measure acceleration. This is accomplished by launching light from a laser into an optical fiber or birefringent crystal slab (double refracting crystal), straining the optical fiber/birefringent crystal via a proof mass acting as the acceleration transducer mechanism, and measuring the resultant phase change due to a fiber/crystal length change and an index of refraction change. This resultant phase change through optical interference manifests itself into an intensity change measurable via a photodetector. Fiber-optic accelerometer systems promise revolutionary breakthroughs in acceleration sensitivity. Foremost, their dynamic range is theoretically at the 10^{10} level⁴ -- limited only by photon shot noise, and electrical noise. This dynamic range can be traded off for environmental induced system biases (temperature, acoustic, and magnetic biases), and still retain a 10^7 or better dynamic range. As biases are reduced through technological

developments, sensitivity for fiber-optic accelerometer systems has room to improve, whereas, pendulous servo-force rebalance accelerometer and vibrating element accelerometer systems have almost reached theoretical limitations. Secondly, the promise of an all fiber-optic inertial guidance and navigation system, i.e., integrated fiber-optic gyro and accelerometer system, utilizing a common optical path, will further increase system reliability and performance. Furthermore, fiber-optic systems are much simpler systems, incorporate no moving parts, have a strong potential for miniaturization through integrated circuitry/optical technology, have almost instantaneous start-up times, require very little power, and are projected to be relatively inexpensive. The following section will discuss several very promising fiber-optic accelerometer approaches as well as select one approach (CSDL proposed concept) for preliminary analysis.

1.2 Thesis Outline

The main emphasis of this thesis is the experimental investigation of a Charles Stark Draper (CSDL) proposed fiber-optic accelerometer concept. As part of the experimental investigation, a particular single-mode fiber type (high or low birefringent fiber), accelerometer cylinder material and dimensions will be defined, and a system scale factor and bias offset will be identified. Major concept demonstrations will include a single as well as dual fiber/PZT cylinder polarization, phase and temperature stability characterization, optical common-mode rejection of thermal effects, and differential sensing of acceleration with optical common mode rejection.

Chapter #2 briefly describes state of the art accelerometer performance and surveys the most viable current fiber-optic accelerometer systems/concepts to date. The advantages and disadvantages of each fiber-optic accelerometer system are identified and the emergence of the CSDL fiber-optic accelerometer concept/configuration is shown.

Chapter #3 addresses the theory of operation of the CSDL fiber-optic accelerometer concept, starting by introducing birefringence and its different types utilized in the CSDL fiber-optic accelerometer. The manifestations of a change in birefringence and fiber length in terms of phase change will be explored and a drum to fiber transduction equation leading to a scale factor determination will be developed. This will be followed by a description of an ac modulation approach for sensing acceleration.

Chapter #4 will experimentally test the CSDL fiber-optic accelerometer system to determine the type of single-mode fiber to be used, the cylinder material, and dimensions needed. A single and double cylinder wrapped with single-mode fiber will be characterized as to polarization, phase, and temperature stability. Optical common mode rejection will be tested and the performance level determined. Finally, differential acceleration sensing will be experimentally investigated.

Chapter #5 will discuss test results and integrate these with theoretical predictions.

Chapter #6 will summarize the experimental findings, and will make recommendations for further research to develop the CSDL fiber-optic accelerometer concept into a viable instrument.

CHAPTER 2

REVIEW OF FIBER-OPTIC ACCELEROMETER SYSTEMS

2.1 Introduction

Several novel fiber-optic accelerometers will be discussed below. Advantages and disadvantages of each system will be specified. Finally, a concept will be chosen (CSDL proposed concept) for preliminary analysis and eventual implementation.

2.2 Mitsubishi Corp., Photoelastic Effect Fiber-Optic Accelerometer⁵

This fiber-optic accelerometer utilizes a rectangular slab of isotropic epoxy resin as the photoelastic/birefringent material. Light is utilized from a laser diode connected to a small length of multi-mode optical fiber terminated with a graded index rod lens for light collimation. The collimated light is then linearly polarized at 45 deg via a high quality linear polarizer and propagated at 45 deg through the photoelastic material upon which a proof mass is placed. As an ac vibration, simulating acceleration is applied to the proof mass in the direction of sensitivity (vertical direction), stress-induced birefringence in the photoelastic material results. Due to this stress-induced birefringence, two orthogonal polarization modes with different indices of refraction, and, hence different light velocities propagate in the epoxy resin along the x_1 and x_3 direction as shown in Figure 1. By injecting light at 45 deg, both modes are propagated, and as a result, initially linearly polarized light is changed to elliptically polarized light by the photoelastic material. Consequently, light reaching the analyzer becomes intensity modulated. The analyzer is also placed at 45 deg relative to the vertical to interfere the two orthogonal polarizations. A quarter wave plate is placed in front of the analyzer to induce a 90 deg phase shift acting as an optical bias for the system. The now intensity-modulated light is

coupled into the outgoing fiber via a second graded index rod lens and propagated to a photodiode. The electrical signal converted by the photodiode is in proportion to the applied stress generated by the vibrational acceleration. See Figure 2 for system configuration. Hence, the sensed quantity is acceleration induced stress in the photoelastic material, which induces a resultant phase change

$$\Delta\phi = \frac{2\pi lCT}{\lambda_0} \quad (1)$$

where

- l = slab length
- C = photoelastic constants for the epoxy resin
- T = stress applied (Force/Area) and
- λ_0 = free space wavelength.

This phase change ($\Delta\phi$) when combined with an ac applied force is equal to

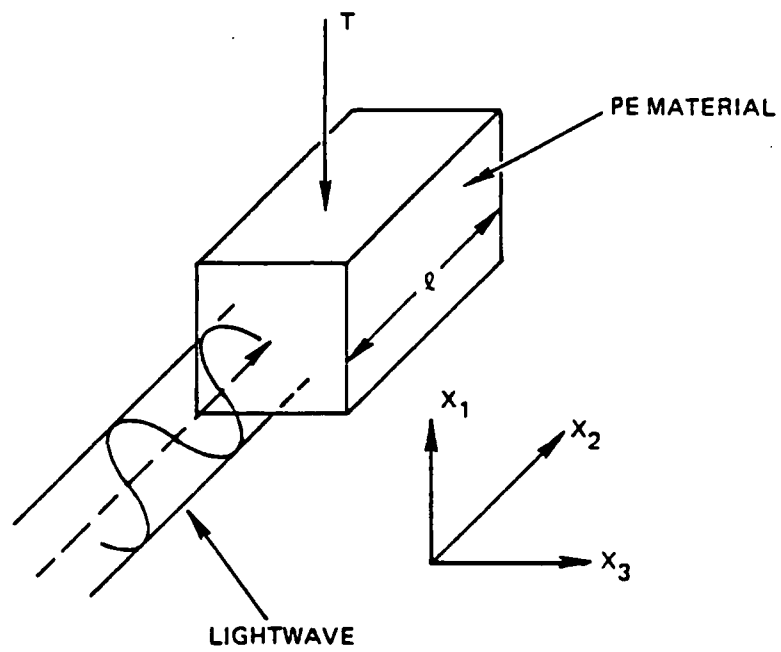
$$\Delta\phi = \frac{2\pi lCT}{\lambda_0} (1 - \alpha \sin \omega t) \quad (2)$$

where

- $\alpha = \omega^2 A/g$ = measured acceleration
- ω = angular vibration frequency
- A = ac amplitude
- g = acceleration of gravity

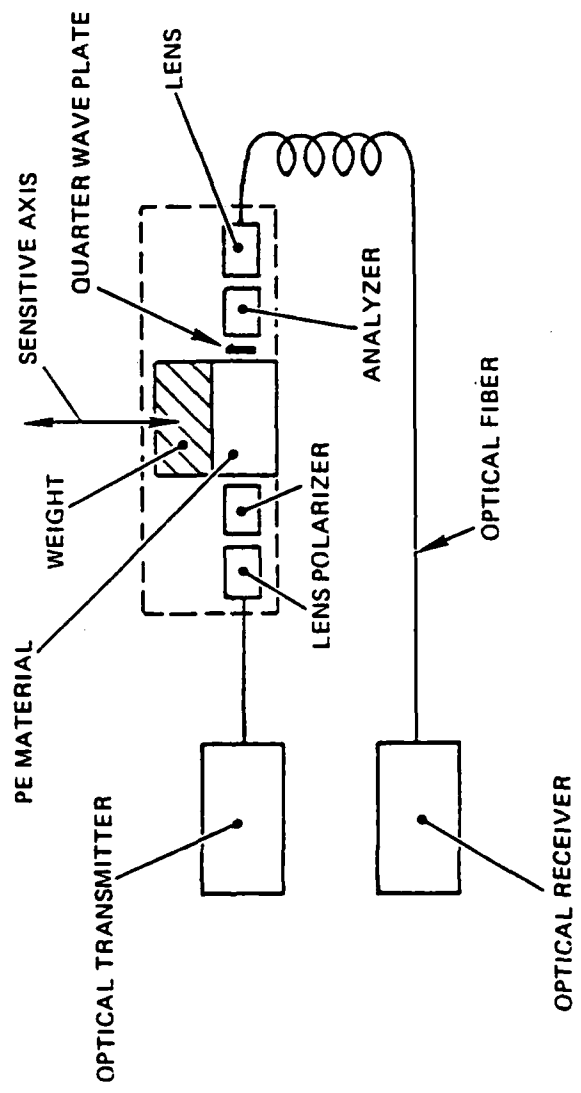
Hence, the detector measured quantity of intensity is

$$I = I_0/2 (1 + \sin \Delta\phi). \quad (3)$$



TSA 5522

Figure 1. Orthogonal polarization mode propagation in an epoxy resin sample.



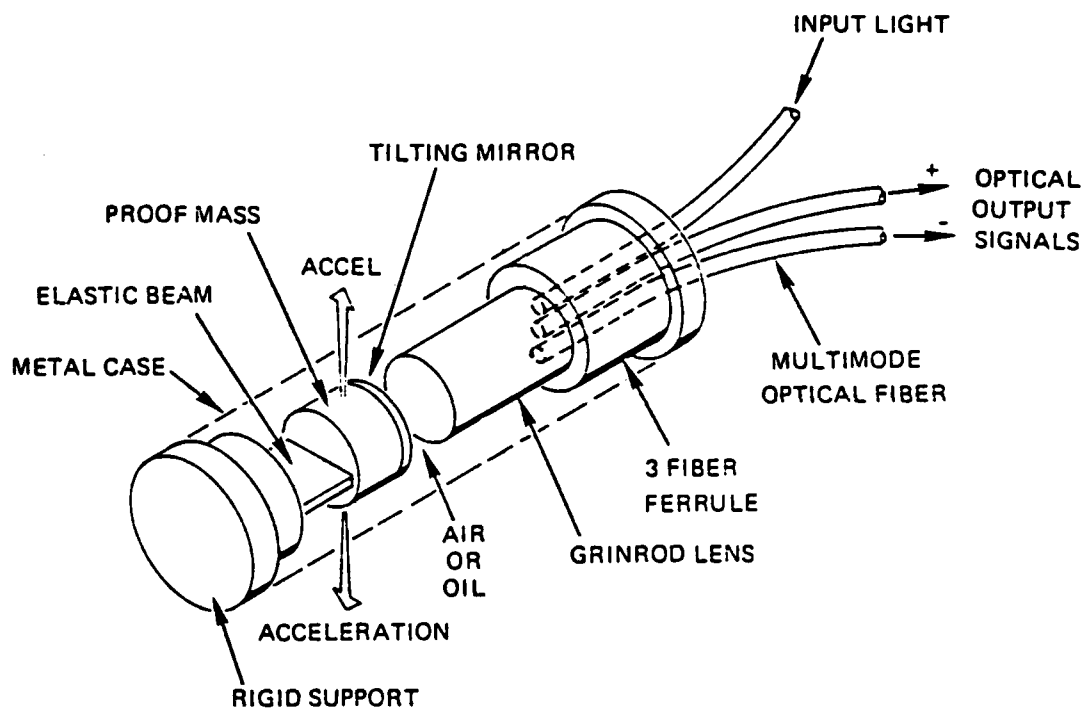
TSA 5523

Figure 2. Mitsubishi Corporation photoelastic effect fiber-optic accelerometer configuration.

This fiber-optic accelerometer senses acceleration from 10^{-3} to 30 g in a frequency range of dc to 3 kHz. Its advantages are: 1) a relatively simple to implement system with moderate performance, and 2) good linearity up to a 10^4 dynamic range at frequencies up to 3 kHz using epoxy resin, but higher ($\approx 10^6$ dynamic range) using solithane 113. Its disadvantage is the high degree of temperature dependence; sensitivity variation is as high as $\pm 10\%$ in a temperature range of -10°C to 40°C due to material natural birefringence caused by residual stress concentrations. System temperature dependence can be improved by developing appropriate small residual stress photoelastic materials. Further disadvantages are the use of high loss optical fiber (multi-mode), bulk optic components and no system quadrature locking.

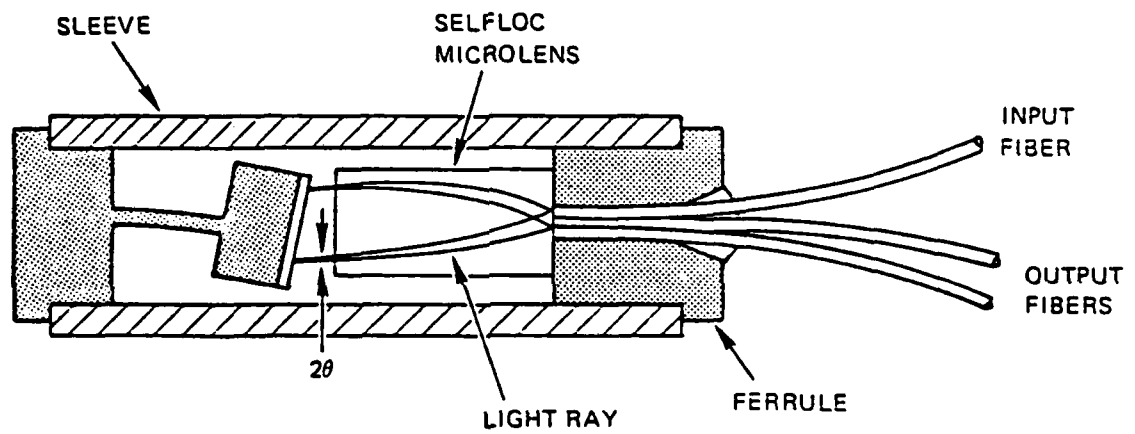
2.3 Tilting-Mirror Fiber-Optic Accelerometer⁶

The tilting-mirror fiber-optic accelerometer consists of a mass-loaded elastic beam assembly and a fiber-optic assembly which reads out the deflection that occurs when an external force is applied to the beam. Figures 3 and 4 show the structure and assembly of the sensor. Three multi-mode fibers are cemented into a brass ferrule whose end is optically polished in order to serve as the optical input-output surface. A quarter pitch graded index rod lens is attached to the ferrule, collimating the laser light from the input fiber, prior to light hitting the mirror polished surface of the proof mass. The proof mass is attached to a cantilevered brass beam whose height is less than its width, thus, deflecting freely up and down, but reflecting very little in the cross axis or horizontal direction. The cantilevered mirror deflects due to induced acceleration in its sensitive axis causing the light from the graded index rod lens to strike the mirror at an angle θ with respect to the mirror normal and reflects back at an angle 2θ into the graded index rod lens. The graded index rod lens again collimates the light and focuses it on the two output fiber ends in the ferrule. The center of the input fiber is situated at a distance $+x$ above the graded index rod lens, while the image is situated at $-x$. The reflected image light falls at a location midway between the two



TSA 5524

Figure 3. Tilting-mirror fiber-optic accelerometer sensor structure.

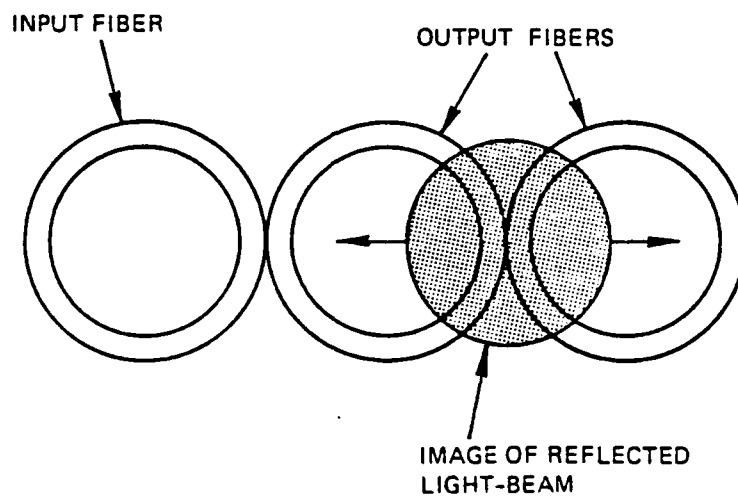


TSA 5525

Figure 4. Tilting-mirror fiber-optic accelerometer functional drawing.

output fibers as shown in Figure 5, so equal portions of light fall on the two fiber ends when the induced acceleration is zero. If acceleration is induced (depending on direction), the focal spot of the reflected light beam is displaced causing an unequal amount of light falling on one of the two output fibers. This light intensity change is detected by a photodetector and scaled to the induced acceleration. This device has a minimum detectable acceleration of 2.4×10^{-6} g rms and a maximum measurable acceleration of 39 g rms (a 10^7 dynamic range). The tilting-mirror fiber-optic accelerometer's limitations are:

- (1) cantilever beam material hysteresis;
- (2) maximum beam deflection angle limited by cantilever beam dynamics;
- (3) light loss at graded index to fiber junction due to high numerical aperture mismatch between the two, (large graded index lenses are not made with fiber compatible numerical apertures);
- (4) utilization of lossy multi-mode fiber;
- (5) fiber and cantilever beam temperature change susceptibility;
- (6) significant fiber bending noise at dc and very low frequencies due to uneven fiber deformation,



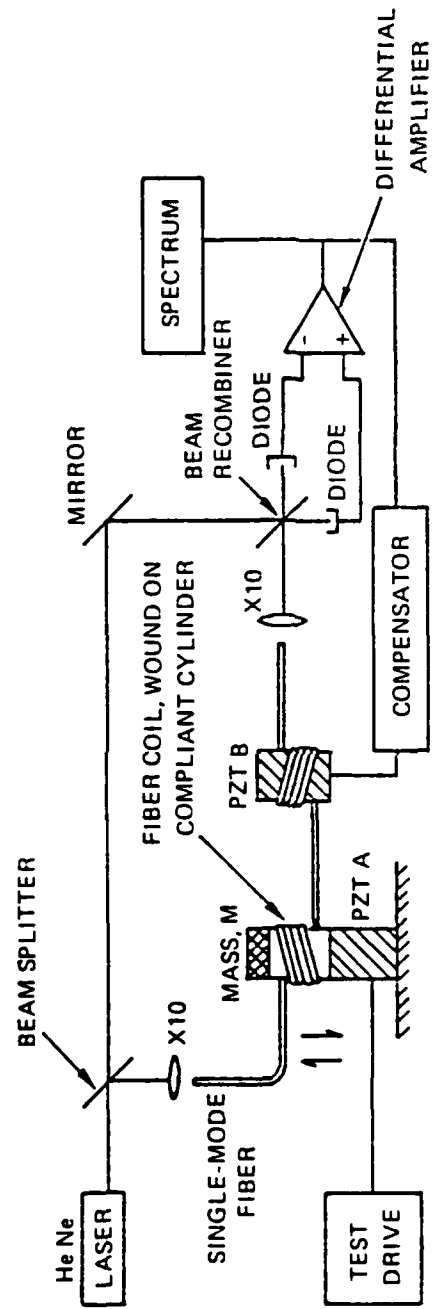
TSA 5526

Figure 5. Tilting-mirror fiber-optic accelerometer light profile at zero induced acceleration.

2.4 Solid/Hollow Cylinder Fiber-Optic Accelerometer⁴

This fiber-optic accelerometer utilizes a Mach-Zender interferometer approach in combination with a low birefringent single-mode fiber, tension wrapped around a cylindrical drum, and an active compensation system for sensing acceleration (see Figure 6). Light from a HeNe laser is beam split via a 50/50 beamsplitter with one path acting as the reference and the other the sensing arm. The sensing arm composed of linearly polarized light is then focused into a single-mode fiber via a 10X lens. This single-mode fiber is wrapped in tension around a small diameter cylinder supporting a proof mass. Tension wrapping a single mode fiber induces a large birefringence into the fiber which is orientated parallel and perpendicular to the cylinder axis. This allows the propagation of two orthogonal polarization modes in the fiber. The proof mass on top of the cylinder acts as a transducer mechanism for transforming induced acceleration into a radial displacement of the cylinder walls. This cylinder deformation induces a strain into the fiber which stretches the fiber and causes a simultaneous optical fiber length change and index of refraction change. This results in an overall phase change of the light propagating in the fiber. The fiber birefringence and strain effect will be discussed in more detail later in this paper. Light exiting from the fiber is optically interfered with the reference beam (after collimation by a second 10X lens) via a second 50/50 beamsplitter. The light intensity is then converted to a current via a photodetector and fed to a differencing amplifier and measured. An active compensation scheme working off of the differencing amplifier output, and a PZT cylinder wrapped with the same fiber piece, maintains the interferometer operating point at maximum sensitivity (quadrature). A second PZT cylinder driven at ac provides an ac measurement.

This accelerometer displays good linearity as a function of induced acceleration. A detection sensitivity of 10^{-10} g or dynamic range of 10^{10} may be theoretically achieved utilizing sufficiently compliant material. Several other advantages are:



TSA 5527

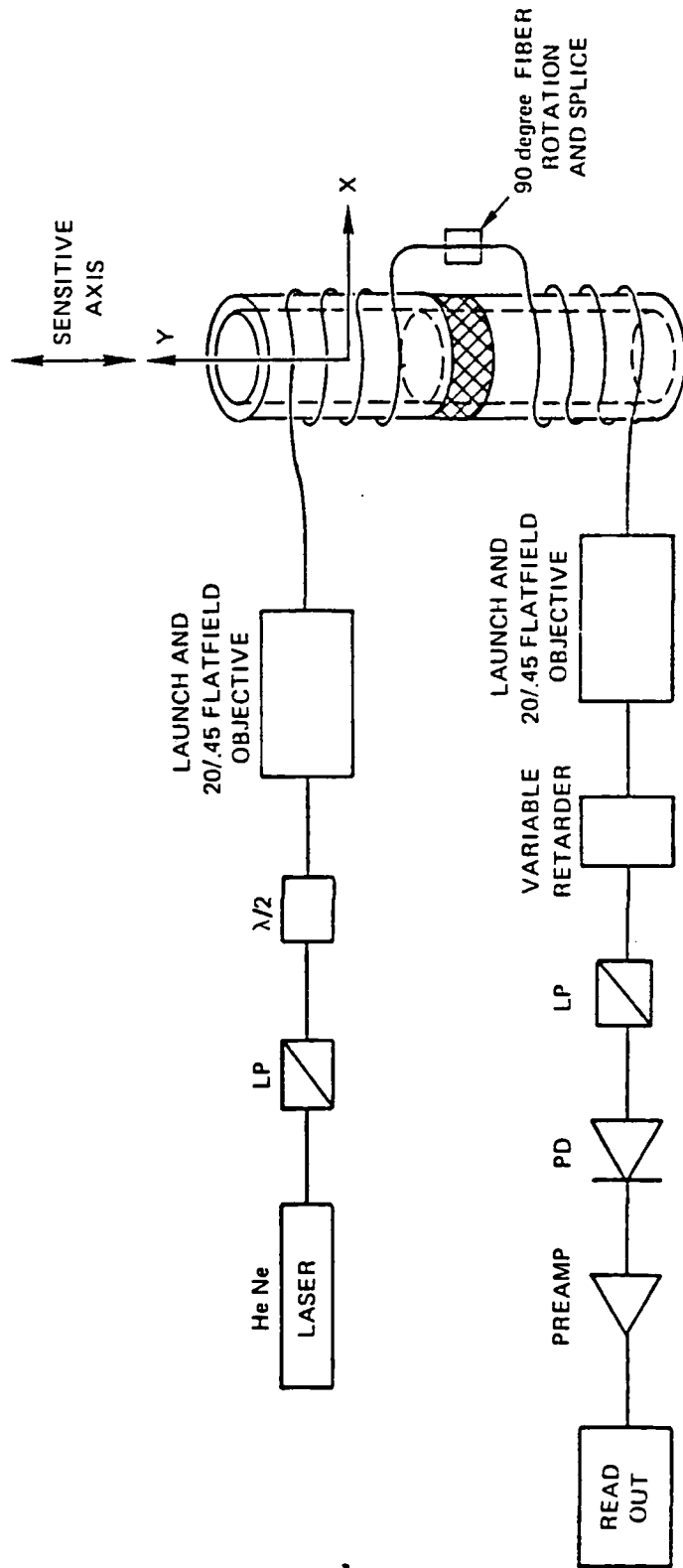
Figure 6. Solid/hollow cylinder fiber-optic acceleration configuration.

- (1) its controllable sensitivity via number of fiber turns around the cylinder;
- (2) reduced lateral (perpendicular to accelerometer sensing axis) acceleration sensitivity;
- (3) controllable resonance frequency via cylinder wall thickness, cylinder compliance, and proof mass size.

However, even with active compensation environmental effects (primarily temperature, pressure, and magnetization effects) are not totally eliminated. Furthermore, the input polarization state is not adequately controlled for launching into the two orthogonal polarization modes causing unnecessary sensitivity of the fiber to environmental perturbations.

2.5 CSDL Fiber-Optic Accelerometer Concept

The CSDL two drum fiber-optic accelerometer is similar to the previously mentioned solid/hollow cylinder fiber-optic accelerometer (see Figure 7 for the CSDL two drum fiber-optic accelerometer system). Two hollow cylinders, stacked one on top of another, and separated by a proof mass, are wrapped with single-mode fiber. As an acceleration is induced along the sensitive axis of the system, the acceleration transmitted to the two hollow cylinders via the proof mass acting as a transducer mechanism causes one cylinder to experience a radial outward displacement and the other cylinder to experience a radial inward displacement. This push-pull concept of common mode rejection will be utilized to eliminate environmental perturbations in a similar manner as the vibrating beam quartz crystal accelerometer mentioned earlier. Common mode rejection of environmental perturbations is achieved via a 90 deg fiber rotation and splice at the fiber midpoint. A second major refinement is the utilization of the single-mode fiber orthogonal polarization states as the reference and sensing paths of the interferometer, eliminating the external reference path utilized by the



TSA 5528

Figure 7. CSDL fiber-optic accelerometer concept with optical common mode rejection.

single drum system previously mentioned. Here optical interference will be conducted by mixing of the two orthogonal polarization modes via an analyzer (Glan Thompson Linear Polarizer) set at 45 deg relative to the fiber output polarization basis. Further, system refinements include:

- (1) closely controlled vertically polarized light entering the 50/50 beamsplitter for minimum polarization state perturbation;
- (2) launching of highly linear light at 45 deg into both orthogonal polarization modes via a Glan Thompson Linear Polarizer, a polarization rotator, and a flat field 20X microscope objective, respectively; and
- (3) a variable retarder for quadrature operation.

This system seems to be the most promising since replacement of bulk optic components with corresponding all-fiber components is possible,⁷ and common moding of environmental perturbations should improve performance considerably. For these reasons, the CSDL two drum fiber-optic accelerometer concept has been chosen for concept analysis and development.

CHAPTER 3

THEORY OF OPERATION OF THE CSDL FIBER-OPTIC ACCELEROMETER CONCEPT

3.1 Introduction

This chapter discusses the theory behind the operation of the CSDL Fiber-Optic Accelerometer. Fiber birefringence will be introduced, the system phase change due to induced acceleration will be calculated, a drum to fiber transduction model derived, and a system scale factor and bias calculated. An ac differential signal modulation scheme will also be briefly discussed.

3.2 Fiber Birefringence and Its Application to the CSDL Fiber-optic Accelerometer Concept

Polarized light (defined by the phase and amplitude of the propagating electric field) propagating through a single-mode fiber experiences a change in polarization state when traversing an area of birefringence in the fiber. Birefringence in a fiber is the anisotropic refractive index distribution in the fiber core region resulting from a geometrical deformation of the fiber core, or a material anisotropy induced through various elasto-optic, magneto-optic, or electro-optic index changes.⁸ Depending on the alignment of the fiber modes, the induced birefringence modes, and the relative strength of the induced birefringence, the polarization modes may or may not couple. Hence, any single-mode fiber used as a sensor is highly unstable due to its susceptibility to environmentally-induced perturbations (microbending, curvature, lateral pressure, etc., varying with temperature and vibration).

In order to overcome these shortcomings and utilize single-mode optical fiber as a sensor, two avenues are available:

- (1) Utilizing a very low birefringent fiber and artificially inducing a strong birefringence (β_{tc}) via tension coiling the fiber around a cylindrical former, thus aligning the fiber β_{tc} mode axes automatically (perpendicular and parallel to the coil axes) with the induced additional birefringence axes. The induced additional birefringence results from the cylinder radius change as well as the cylinder axial strain. Thus, the fiber experiences an axial as well as transverse stress, respectively. The cylinder axial strain when imparted into the fiber has been found to be the dominant effect.⁹

- (2) Initially utilizing high birefringent fiber with already strongly established polarization modes. If the high birefringent fiber is tension coiled around a cylindrical former care must be taken to align the fiber internal birefringence (β_i) axes with that of the induced additional birefringence due to cylinder axial strain (β_f). If the β_i axis is aligned with the β_f axis a change in β_f corresponds to a large change in β_i , making the fiber approximately 20 times more sensitive than in the low birefringent tension coiled case.¹⁰ However, if the high birefringent fiber is tension coiled and no care is taken to align the β_i axes with the β_f axes, the β_f effect will subtract from β_i and very low fiber sensitivity can be experienced.¹⁰ If, on the other hand, the high birefringent fiber is loosely wrapped with just enough tension to prevent sliding on the cylinder, and no regard to orientation is observed, the compliant fiber outer jacket buffers the fiber core and cladding from experiencing any external transverse stress. The remaining effect, fiber axial strain due to cylinder radius change, has no specific axis preference and thus serves to

reinforce β_1 . The overall fiber sensitivity is only (utilizing a bare high birefringent fiber) approximately 7 times greater than the low birefringent tension coiled fiber.¹⁰

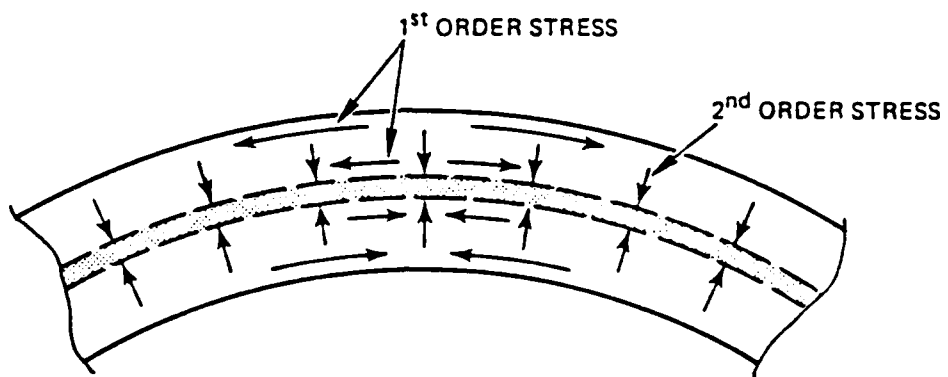
Both methods rely on the fact that if the fiber modes and the induced birefringence modes are aligned, the fiber birefringence will only be changed and no polarization coupling will take place. This change in birefringence and hence measured intensity will serve as the acceleration sensing mechanism in the two drum fiber wrapped cylinder concept.

3.3 Origin and Types of Birefringence Mechanisms Contributing to the Light Phase Delay in the CSDL Concept

3.3.1 Bending Birefringence

A linear birefringence can be induced into a fiber by bending the fiber.¹¹ The first order stress of a bent fiber is tangential to the fiber causing the exterior of the fiber to be in tension and the interior to be in compression. This first order effect is very small in the center of the fiber where the guided mode is nonzero. Furthermore, it affects both polarizations the same, and therefore, induces no difference between their propagation constants, and hence, no birefringence (see Figure 8 for the first and second order stresses). The second order stress is in the plane of the bend and perpendicular to the fiber. It is a maximum near the center of the fiber and vanishes at the boundaries.¹¹ It therefore induces a birefringence in the fiber with its fast axis in the plane of the bend. The birefringence from the second order transverse stress is

$$\beta_b = 0.25 k_o n^3 (\rho_{11} - \rho_{12}) (1 + \mu_f) K^2 r^2 \text{ rad/m} \quad (4)$$



TSA 5529

Figure 8. Bending birefringence.

where

- $k_0 = 2\pi/\lambda_0$
- ρ_{11} and ρ_{12} = fiber strain optic tensor elements
- μ_f = Poisson's ratio of the fiber
- $K = 1/R_1$
- R_1 = radius of curvature of the bend
- r = radius of the fiber.

Using typical material constants for fused silica,¹² ($n = 1.46$, $\mu = 0.17$, $[\rho_{11} - \rho_{12}] = -0.15$ and $\lambda_0 = 0.633 \mu\text{m}$), a bending birefringence of

$$\beta_b = -1.34 \times 10^6 K^2 r^2 \text{ rad/m} \quad (5)$$

is obtained. This result holds universally for weakly guided silica fiber, regardless of their core diameter and index profiles.¹¹ For large radius of curvature bends, this birefringence is small (large polarization beat length, $L_p = 2\pi/\beta_b$); however, for very small bending radii where $2R_1 = 1 \text{ cm}$, very large birefringences can be seen with L_p of several centimeters.⁸ For accelerometer sensor application, these small coil diameters ($2R_1 = 1 \text{ cm}$) are somewhat impractical. However, more practical coil diameters of 3.0 to 6.0 centimeters can be obtained with very high birefringence by simply tension wrapping a single-mode fiber around a cylindrical drum. This concept will be explored next.

3.3.2 Tension - Coiling Birefringence

Strong birefringence can be induced into a single-mode fiber by coiling the fiber under tension around a cylindrical former as shown by Rashleigh.¹³ Tension-coiling birefringence is very similar to bending birefringence. There is no first order stress effect due to symmetry. Furthermore, when a straight fiber is subjected to pure tensile stress,

inducing an axial strain, no birefringence is induced. However, when a fiber is subject to a simultaneous bending and tension, a second order mixing of the first order bending and tensile stress effects occur, producing a second order birefringence proportional to the radius of curvature of the bend and the induced strain, with the fast axis automatically aligned with the radius of curvature. If either the bending element or the axial strain vanish, the birefringence due to tension-coiling also vanishes.¹³ This birefringence is characterized by Rashleigh¹³ and can be written as

$$\beta_{tc} = 0.5 k_o n^3 (\rho_{11} - \rho_{12}) (1 + \mu_f) \left(\frac{2 - 3\nu}{1 - \mu_f} \right) K r \epsilon_z \text{ rad/m} \quad (6)$$

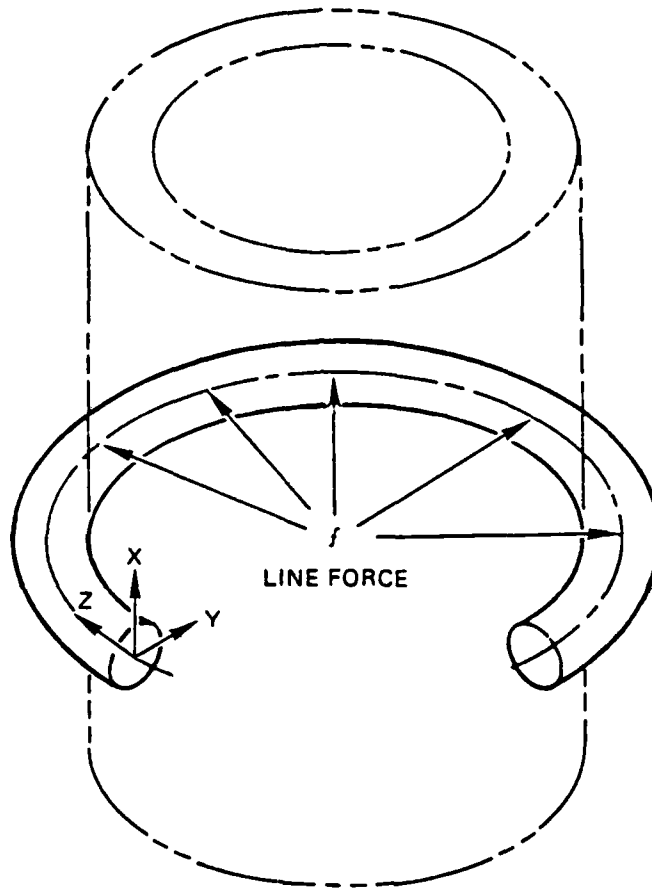
where the parameters are the same as Equation (4) with ϵ_z being the applied strain. For a single-mode fiber Equation (6) becomes:

$$\beta_{tc} = -4.89 \times 10^6 K r \epsilon_z \text{ rad/m.} \quad (7)$$

Using this approach yields polarization beat lengths of 2.0 to 5.0 cm for cylindrical formers of 3.0 to 6.0 cm in diameter with approximately 1 to 4% axial strain (ϵ_z).

3.3.3 Transverse Stress Birefringence

The action of the cylinder axial strain (as a result of induced acceleration) results in the transfer of a transverse stress to the fiber wrapped around the cylinder. The transverse fiber stress can be expressed as a transverse strain produced by the action of an equal and opposite transverse force, f , (per unit fiber length) acting as a sharp line force concentrated along the fiber. Figure 9 depicts this force.



TSA 5530

Figure 9. Transverse stress birefringence.

The birefringence induced by this force is characterized by Rashleigh⁹ as

$$\beta_f = \frac{8}{\pi} k_o \frac{n^3}{2E_f} (\rho_{11} - \rho_{12}) (1 + \mu_f) \frac{f}{2r} \text{ rad/m} \quad (8)$$

where

$$\begin{aligned} r &= \text{fiber outer radius} \\ E_f &= \text{Young's modulus for the silica fiber} \\ f &= 2rE_f \epsilon_y \end{aligned}$$

with ϵ_y being the fiber strain in the y direction, i.e., along the direction of the acting force. This reduces to

$$\beta_f = -6.93 \times 10^6 \epsilon_y \text{ rad/m.} \quad (9)$$

3.3.4 Internal Birefringence of a High Birefringent Single-Mode Fiber

Core ellipticity alone can introduce a large internal fiber birefringence but the core must be very small; 2a (the semi-major axis) must be $\leq 2.4 \mu\text{m}$ and 2b (the semi-minor axis) must be $\leq 0.8 \mu\text{m}$ to be within the single-mode regime.¹⁴ This makes launching light into the core very difficult. A more practical approach to achieving high internal birefringent fibers is to utilize a stress producing dopant (usually boron) within a circular silica substrate (yielding 4 to 5 μm core diameters). A variety of these stress-doped fibers exist (elliptical, circular side pit, bow tie, etc.); however, only one configuration maximizing the internal birefringence and being the optimum structure is the 90 degree stress-lobe bow tie configuration.¹⁵ Hence, a bow tie fiber will be used for part of the experimentation in this report. The internal or thermal stress birefringence in a high birefringent stress lobed fiber is the result of

a difference in Poisson's ratio and a difference in thermal expansion coefficients of the component glasses (dopant and silica) from which the fiber is constructed.^{15,16} The internal birefringence is calculated by [15] utilizing Timoshenko¹⁷ to solve the partial differential equation for plane strain in a body with circular cross-section and internal stresses. The solution is the sum of the particular integral and the complementary function and is written as

$$B_i = -\frac{CE_f T}{1 - \mu_o} \int_{0.1}^1 \frac{1}{\pi} \int_0^{2\pi} \alpha(r, \theta) \cos 2\theta d\theta (r^{-1} - 3r^3) dr \quad (10)$$

where

- C = stress optic coefficient
- E_f = Young's Modulus of the fiber
- T = difference between ambient temperature and the lowest fictive temperature (point at which the component glass sets) of the glasses within the fiber
- μ_o = Poisson's ratio at the core
- r = normalized outer radius of the fiber
- $\alpha(r, \theta)$ = expansion coefficient profile in polar coordinates

This equation assumes a symmetrical fiber cross-section and a small variation of E_f and μ_f across the fiber cross-section. Upon inducing a cylinder radius change and thus straining the fiber axially (along the z direction), free strains in the transverse x and y direction are induced, i.e., $\epsilon_x = \epsilon_y = -\mu_f \epsilon_z$. These are comparable to the thermal strains and hence, $\epsilon_x = \epsilon_y = \alpha T$. Also for the bow-tie fiber θ is constant, hence Equation (10) can be rewritten as

$$B_i = \frac{CE_f}{1 - \mu_o} \frac{2}{\pi} \Delta \alpha T \int_{0.1}^1 \sin 2\phi (r^{-1} - 3r^3) dr \quad (11)$$

with ϕ being the angle at which the stress-lobe region intersects the circle of radius, r . Keeping the stress lobes at $2\phi = 90$ degrees (bow-tie orientation), relatively small and close to the center of the fiber yields a solved equation of

$$\beta_i = - \frac{4CE_f \Delta\alpha T}{\pi(1 - \mu_o)} \quad (12)$$

where

$\Delta\alpha$ = difference in expansion coefficients of the two glasses

μ_o = Poisson's ratio of the fiber at the core.

Utilizing $\epsilon_y = -\Delta\mu_f \epsilon_z$ and $\epsilon_y = \Delta\alpha T$ to relate ϵ_z to the difference in expansion coefficients and the difference in Poisson's ratio ($\Delta\mu_f$) for the two glass components, we have

$$\epsilon_z = - \frac{\Delta\alpha T}{\Delta\mu_f} \quad (13)$$

and now Equation (12) becomes

$$\beta_i = \frac{4CE_f \Delta\mu_f \epsilon_z}{\pi(1 - \mu_o)} \quad (14)$$

where CE_f is equivalent to Rashleigh's⁸ C_s (strain optic coefficient) and is

$$C_s = 0.5 k_o n_o^3 (\rho_{11} - \rho_{12}) (1 + \mu_f) \quad (15)$$

with $k_c = 2\pi/0.633 \mu\text{m}$, $n_o = 1.46$, $\rho_{11} - \rho_{12} = -0.15$ and $\mu_f = 0.17$, a value of $C_s = -2.71 \times 10^6$ is obtained. Further utilizing $\Delta\mu_f = 0.02$ and $\mu_o = \mu_f = 0.17$ we have

$$\beta_i = -8.32 \times 10^4 \epsilon_z \text{ rad/m.} \quad (16)$$

3.4 $\Delta\beta$ and ΔL Contributions to Phase Change in the CSDL Concept

In order to understand how an acceleration induced stress via the hollow cylindrical drum system changes the light phase and hence measured intensity after interference of the two orthogonal polarization modes, two cases need to be explored:

- (1) the cylinders wrapped with tension coiled single-mode low birefringent fiber, and
- (2) the cylinders wrapped with single-mode nontension coiled high birefringent fiber.

In both cases the phase of an unperturbed light wave with time dependence (ωt) suppressed is

$$\phi = \beta L \quad (17)$$

where

- $\beta = k_o (n_x - n_y)$ = the fiber birefringence
 k_o = the free space fiber propagation constant equal to $2\pi/\lambda_o$ with λ_o being the free space wavelength
 n_x and n_y = the refractive indices of the two polarization modes propagating in the fiber
 L = the respective fiber length.

The induced acceleration is transferred to the individual cylinders via the actions of the proof mass transducer. The effect is a cylinder radius change and a cylinder axial strain. These cylinder effects cause the fiber to experience a longitudinal strain (along the fiber length) and a transverse (across fiber cross-section) stress, respectively. Either one or both of these cylinder effects can cause the phase at the output end of the fiber to change by inducing additional birefringence into the fiber. Hence,

$$\Delta\phi = \Delta(\beta L) = \beta\Delta L + L\Delta\beta \quad (18)$$

where:

$\Delta\beta$ = the change in the fiber birefringence and is equal to $k_0(\Delta n_x - \Delta n_y)$ and

ΔL = the fiber length change.

Rashleigh¹⁰ has shown, by normalizing $\Delta\phi$ as to L and ΔL and straining a single-mode fiber axially, that $\Delta\beta$ is approximately 30 times larger than the β effect and hence the second term is larger than the first. Assuming that no second-order mixing of the birefringences occur, the fiber birefringences can be postulated to be linear and hence can be added or subtracted depending on the action of the stimulus. Furthermore, since the birefringences are linear, the resulting phase changes are also additive

$$\Delta\phi_{TOTAL} = \Delta\phi_{tc} + \Delta\phi_f + \Delta\phi_b + \dots \quad (19)$$

with the total phase change reflecting the phase effect of each birefringence mechanism.

3.4.1 Linear Combination of Resultant Phase Changes Due to Birefringence Mechanisms for the Tension Coiled Low Birefringent Fiber Case

In this case birefringences due to tension coiling, bending, and transverse strain are present, i.e., β_{tc} , β_b and β_f . Hence four separate phase changes ($\Delta\phi_{tc}$, $\Delta\phi_b$ and $\Delta\phi_f$), comprise the overall total system induced phase change. These can be looked at separately:

- (1) $\Delta\phi_{tc}$ -- from Equation (7) with $1/R_1$ (radius of the cylinder), substituted for K we have

$$\beta_{tc}[R_1, \epsilon_z(R_1)] = -4.89 \times 10^6 \frac{r\epsilon_z}{R_1} \text{ rad/m} \quad (20)$$

and the resulting phase change

$$\Delta\phi_{tc} = \left(\beta_{tc} \frac{dL}{dR_1} + L \frac{d\beta_{tc}}{dR_1} \right) \Delta R_1 \quad (21)$$

and differentiating β_{tc} implicitly with respect to R_1

$$\frac{d\beta_{tc}}{dR_1} = 4.89 \times 10^6 \frac{r\epsilon_z}{R_1^2} - 4.89 \times 10^6 r/R_1 \frac{d\epsilon_z}{dR_1} \quad (22)$$

Now, defining

$$\epsilon_z = \frac{dL}{L} \quad \text{and} \quad \epsilon_\theta = \frac{dR_1}{R_1} \quad (23)$$

and equating cylinder radial change to fiber axial change we have

$$\epsilon_{\theta} = \epsilon_z. \quad (24)$$

Furthermore, assuming that $\frac{d\epsilon_z}{\epsilon_{\theta}} \approx 1$, i.e., the change in strain can be as large as the initial strain, and substituting all of the above equations/definitions into Equation (20) and rearranging,

$$\Delta\phi_{tc} = -4.9 \times 10^6 \frac{Lr}{R_1^2} \Delta R_1 \text{ rad} \quad (25)$$

(2) $\Delta\phi_b$ -- from Equation (5) with $K = 1/R_1$ we have

$$\beta_b(R_1) = -1.34 \times 10^6 \frac{r^2}{R_1^2} \text{ rad/m} \quad (26)$$

differentiating with respect to R_1 we have

$$\frac{d\beta_b}{dR_1} = 2.68 \times 10^6 \frac{r^2}{R_1^3}. \quad (27)$$

Now applying Equation (21) and making the previous simplifying assumptions

$$\Delta\phi_b = 1.34 \times 10^6 \frac{Lr^2}{R_1^3} \Delta R_1 \text{ rad.} \quad (28)$$

(3) $\Delta\phi_f$ -- from Equation (9)

$$\beta_f(\epsilon_y) = -6.93 \times 10^6 \epsilon_y \text{ rad/m} \quad (29)$$

differentiating with respect to ϵ_y we have

$$\frac{d\beta_f}{d\epsilon_y} = -6.93 \times 10^6. \quad (30)$$

Now substituting into

$$\Delta\phi_f = \left[\beta_f \frac{dL}{d\epsilon_y} + L \frac{d\beta_f}{d\epsilon_y} \right] \Delta\epsilon_y \quad (31)$$

and assuming

$$\frac{\Delta R_1}{R_1} = -\mu_c \Delta\epsilon_y \quad (32)$$

where μ_c is Poisson's ratio of the cylinder converting the cylinder axial strain into a fiber transverse stress via $\Delta R_1/R$ parameterization. Further applying $\Delta L/L = \Delta R_1/R_1$, substituting the appropriate values and simplifying, Equation (31) turns into

$$\Delta\phi_f = -6.93 \times 10^6 (1 - \mu_c \epsilon_y) L \Delta\epsilon_y \text{ rad.} \quad (33)$$

Hence, the total system phase change experienced becomes

$$\Delta\phi_{\text{TOTAL}} = -4.9 \times 10^6 \frac{LT}{R_1^2} \Delta R_1 + 1.34 \times 10^6 \frac{Lr^2}{R_1^3} \Delta R_1 +$$

$$-6.93 \times 10^6 (1 - \mu_c \epsilon_y) L \Delta \epsilon_y \text{ rad.} \quad (34)$$

Other phase inducing birefringences such as microbending will not be considered since care will be taken to avoid <1 cm radius bends and fiber-to-fiber overlap while wrapping the fiber onto the cylinders.

3.4.2 Linear Combination of Resultant Phase Changes Due to Birefringence Mechanisms for the Nontension Coiled High Birefringent Fiber Case

In the nontension coiled high birefringent fiber case the total change in phase is determined by the internal birefringence of the fiber and the bending birefringence,

$$\Delta\phi_{\text{TOTAL}} = \Delta\phi_i + \Delta\phi_b \quad (35)$$

Since the high birefringent fiber is nontension coiled no transverse stress due to cylinder axial strain is experienced. The fiber plastic outer jacket acts as a buffer agent to dampen any transverse stress. Since the high birefringent fiber cannot readily be wrapped with regard to orthogonal axis orientation any bending birefringence induced will either serve to enhance or degrade overall fiber birefringence. Hence the bending birefringence phase component cannot be accurately modeled and must therefore be eliminated to the greatest extent possible. This is done by limiting the minimum cylindrical drum outside diameter to >3.0 cm. The remaining bending birefringence is relatively small and

can be ignored. In this report cylinder outside diameters >3.0 cm will be considered leaving the internal birefringence to be the prevailing birefringence inducing the phase change. From Equation (17)

(36)

$$\beta_i[\epsilon(R_1)] = -8.32 \times 10^4 \epsilon_z \text{ rad/m and } \frac{d\beta_i}{dR_1} = -8.32 \times 10^4 \frac{d\epsilon_z}{dR_1} \text{ rad/m.}$$

Applying Equation (18)

$$\Delta\phi_i = \left(\beta_i \frac{dL}{dR_1} + L \frac{d\beta_i}{dR_1} \right) \Delta R_1 \quad (37)$$

simplifying and realizing that the stretching of the fiber (longitudinal fiber change) is a direct result of the cylinder radius change we can utilize

$$\epsilon_z = \frac{\Delta L}{L} = \frac{\Delta R_1}{R_1} = \epsilon_\theta \text{ and } \frac{d\epsilon_z}{dR_1} = 1 \quad (38)$$

we have

$$\Delta\phi_{\text{TOTAL}} = \Delta\phi_i = -8.32 \times 10^4 (1 - \epsilon_z) \frac{L}{R_1} \Delta R_1 \text{ rad.} \quad (39)$$

3.5 Drum To Fiber Transduction Equation

In this section a cylindrical drum model relating the cylinder radial change with the phase change equations due to the various birefringence mechanisms covered in the previous sections will be derived. From this model system sensitivity equations will be extrapolated and theoretical performance values calculated. These will be correlated to later experimental results.

The radial displacement (ΔR_1) for a thin-walled cylinder with uniform axial load P_x in Newtons per linear meter can be approximated via the equation for a thin-walled column¹⁸

$$\Delta R_1 = \frac{P_x \mu_c R_{in}}{E_c t} \quad (40)$$

which is valid for cylinders with $R_{in}/t > 10$

where

- μ_c = Poisson's ratio for the cylinder
- E_c = the cylinder's Young's Modulus
- R_{in} = the inside cylinder diameter
- R_1 = the outside diameter
- t = the cylinder wall thickness.

P can be further expressed as

$$P_x = \frac{m \Delta a}{2\pi R_m} \quad (41)$$

where

- m = the applied mass
- Δa = the induced acceleration
- R_m = the cylinder mean radius.

3.5.1 Theoretical Phase Change Prediction for a Nominal Single Aluminum Cylinder Wrapped with Low Birefringence Tension Coiled Fiber

Applying the previous model to the tension coiled low birefringent case the change in phase is

$$\begin{aligned} \Delta\phi_{\text{TOTAL}} = & -4.9 \times 10^6 \frac{Lr}{R_1^2} \frac{m\Delta a \mu_c R_{in}}{2\pi R_m E_c t} + \\ & + 1.34 \times 10^6 \frac{Lr^2}{R_1^3} \frac{m\Delta a}{2\pi R_m} \frac{\mu_c R_{in}}{E_c t} - 6.93 \times 10^6 (1 - \mu_c \epsilon_y) L \Delta \epsilon_y \text{ rad.} \end{aligned} \quad (42)$$

Since $\epsilon_y = f/(2rE_f)$ and f is in the y direction, $-\mu P_x = f_y$, relates the force f on the fiber to an actual axial cylinder stress, and $\Delta R_1/R_1 = -\mu_c \Delta \epsilon_y$ from before.

$$\begin{aligned} \Delta\phi_{\text{TOTAL}} = & -4.9 \times 10^6 \frac{Lr}{R_1^2} \frac{m\Delta a \mu_c R_{in}}{2\pi R_m E_c t} + 1.34 \times 10^6 \frac{Lr^2}{R_1^3} \frac{m\Delta a \mu_c R_{in}}{2\pi R_m E_c t} + \\ & -6.93 \times 10^6 \left(1 + \frac{m\Delta a}{4\pi^2 R_m E_f}\right) L \frac{m\Delta a R_{in}}{2\pi R_1 R_m E_c t} \text{ rad.} \end{aligned} \quad (43)$$

Recalling from the previous section, on nontension coiling high birefringent fiber that cylinder diameters of >3.0 cm should be used. Here we will also utilize cylinders with cylinder diameters of >3.0 cm; hence, bending birefringence can be neglected as a major phase change effect. Also, second order Δa terms will be discarded in the first order $\Delta\phi_{\text{TOTAL}}$ analysis. Equation (43) can now be written as

$$\Delta\phi_{\text{TOTAL}} = - \frac{m\Delta a R_{in}}{2\pi R_1 R_m E_c t} L \left[4.9 \times 10^6 \frac{r\mu_c}{R_1} + 6.93 \times 10^6 \right] \text{ rad.} \quad (44)$$

Now the system scale factor for a tension coiled low birefringent fiber becomes

$$\frac{\Delta\phi_{TOTAL}}{\Delta a} = - \frac{m R_{in}}{2\pi R_1 R_m E_c t} L \left[4.9 \times 10^6 \frac{r\mu_c}{R_1} + 6.93 \times 10^6 \right] \text{ rad.} \quad (45)$$

Utilizing a 1 meter low birefringent York fiber (OD 210 μm), tension coiled around an aluminum cylinder with approximately 3 to 4% longitudinal strain, a cylinder Young's Modulus of $E_c = 7.0 \times 10^{10}$ N/m², $\mu_c = 0.33$, $R_{in} = 2.68$ cm, $R_1 = 3.00$ cm, $R_m = 2.84$ cm, $t = 3.2$ mm and a proof mass of 0.68 kg yields a cylinder sensitivity ($\Delta\phi/\Delta a$) of -1.03 rad/g. This sensitivity is primarily due to fiber transverse stress and is 4 orders of magnitude larger than the contribution to system sensitivity of the tension coiling phase change (-8.43×10^{-4} rad/g).

3.5.2 Theoretical Phase Change Prediction for a Nominal Single PZT Cylinder Nontension Coiled High Birefringence Fiber

Applying the same ΔR_1 equation to the nontension coiled high birefringence case yields

$$\Delta\phi_{TOTAL} = -8.32 \times 10^4 (1 - \epsilon_z) \frac{L}{R_1} \frac{m\Delta a \mu_c R_{in}}{2\pi R_m E_c t} \quad (46)$$

with $\epsilon_z = \epsilon_\theta = \Delta R_1/R_1$, and looking only at the first order Δa effects the system scale factor is

$$\frac{\Delta\phi_{TOTAL}}{\Delta a} = -8.32 \times 10^4 \frac{L}{R_1} \frac{m \mu_c R_{in}}{2\pi R_m E_c t} \text{ rad.} \quad (47)$$

Substituting typical piezoelectric (PZT) cylinder values ($E_c = 4.8 \times 10^{10}$ N/m², $\nu_c = .33$, $R_1 = 2.58$ cm, $R_{in} = 2.05$ cm, $t = 5.52$ mm, and $R_m = 2.32$ cm), along with a .68 kg proof mass and a 3.5 m high birefringent York fiber length into equation (47) yields a theoretical cylinder sensitivity ($\Delta\phi/\Delta a$) of $\approx -1.32 \times 10^{-2}$ rad/g.

A comparison of the nontension coiled high birefringence sensitivity with the tension coiled low birefringence sensitivity (for equal fiber lengths of 1 meter), indicates that the high birefringent case is approximately 3 orders of magnitude smaller than the low birefringent case. This 3 order of magnitude is attributable to fiber jacket axial strain buffering and cylinder material value discrepancies.¹⁹ Ignoring these leaves the high birefringence case approximately 4 times more sensitive than the low birefringence case.

Since $\Delta\phi = 0$ when induced acceleration is zero, the system bias is a direct result of the internal birefringence of the high birefringent fiber. This bias can be calculated as a phase offset equal to $\beta_1 L$. From equations (13), (16), and (17) we have

$$\phi_{\text{bias}} = 8.32 \times 10^4 \left(\frac{\Delta\alpha T}{\Delta\nu_f} \right) L = -3.83 \text{ rad} \quad (48)$$

where $\Delta\alpha T$ is the thermal expansion mismatch equal to -10^{-3} and $\Delta\nu_f$ is the difference in Poisson's ratio equal to 0.02. The fiber length used is 2.3 meters.

3.6 CSDL Fiber-Optic Accelerometer Concept Incorporating Phase Modulation

In order to escape from electrical noise at dc and achieve a more accurate scale factor ($\Delta\phi/\Delta a$) measurement, an ac approach has to be implemented. The approach most easily implemented is to phase modulate the phase difference to be detected via two piezoelectric cylinders and then demodulate at the driving frequency using a lock-in amplifier.

Looking first at one PZT cylinder wrapped with high birefringent single mode fiber unperturbed by any environmentally induced phase perturbations, the two fields propagating along the fiber are

$$E_1 = E_0 e^{i(\omega t + \phi_1)} \quad \text{and} \quad E_2 = E_0 e^{i(\omega t + \phi_2)} \quad (49)$$

with $\phi_{1,2}$ being the acceleration induced phases. Hence, the parameter of interest is $\Delta\phi = \phi_1 - \phi_2$ which is the phase difference due to acceleration. Modulating the propagating fields with the carrier phase

$$\phi_m = A \sin \omega_m t, \quad (50)$$

interfering the two modulated fields via a Glan Thompson linear polarizer oriented 45 degrees relative to the fiber output axis and detecting the fields by a square law detector yields:

$$I = E_1^2 + E_2^2 + 2E_1 E_2 \cos(\Delta\phi + \phi_m) \quad (51)$$

Substituting for ϕ_m we have

$$I = E_1^2 + E_2^2 + 2E_1 E_2 \cos(A \sin \omega_m t + \Delta\phi) \quad (52)$$

and writing the signals as a Fourier series with odd and even Bessel functions we have

$$I = E_1^2 + E_2^2 + 2E_1 E_2 \left[\cos\Delta\phi \left(J_0(A) + 2 \sum_{k=1}^{\infty} J_{2k}(A) \cos 2k\omega_m t \right) + \right. \\ \left. -\sin\Delta\phi \left(2 \sum_{k=1}^{\infty} J_{2k-1}(A) \sin(2k-1)\omega_m t \right) \right]. \quad (53)$$

Now demodulating at ω_m with a lock-in amplifier, synchronized on the ac voltage which drives the phase modulator gives

$$I = E_1^2 + E_2^2 + 2E_1E_2J_0(A)\cos\Delta\phi - 4E_1E_2\sin\Delta\phi J_1(A)\sin(\omega_m t)$$

or (54)

$$I = -4E_1E_2\sin\Delta\phi J_1(A)\sin(\omega_m t).$$

The dc component is ignored since a lock-in amplifier does not respond to dc at its input.

The demodulation sensitivity is maximum when

- (1) linear light is launched at 45 degrees and $|E_1| = |E_2|$,
- (2) $\sin\Delta\phi$ is $\pi/2$ or $3\pi/2$; operation is at the steepest part of the interference curve,
- (3) $J(A) = J_1(C\pi/V_\pi) = J(1.85)$ is maximum at $A = C\pi/V_\pi = 1.85$ rad where C is the peak-to-peak magnitude of the voltage sweep and V_π is the voltage to achieve π phase shift of the PZT, fiber wrapped cylinder on the interference curve.

For a 3.5 m fiber wrapped around a 2.6 cm outside radius, 5.52 mm thick, PZT-5H ($d_{33} = 5.93 \times 10^{-10}$ m/V) piezoelectric cylinder, V_π is 540 volts. This translates into an optimum peak-to-peak voltage sweep amplitude of 318 volts. However, the frequency generator and the ac operational amplifier employed limited the operational frequency to less than 1 kHz and approximately 300 volts p-p before 3 dB roll-off occurred. In our case operation at nonoptimum peak-to-peak voltage sweep amplitudes served to only decrease the modulation depth.

The above analysis also holds when the same fiber is wrapped around two separate cylinders. However, when the same fiber wrapped around the two PZT cylinders is cleaved and rotated 90 degrees for common-mode rejection and a positive dc voltage applied to one cylinder and a negative dc voltage applied to the second cylinder (to simulate a push-pull accelerometer configuration with the \pm dc volts corresponding to a known acceleration level), the differential phase modulation will be zero and no signal modulation will occur:

AC modulation

Signal (I)

Cylinder 1 $I_1 = (\text{dc term}) -4I_0 J_1(A) \sin \omega_m t \sin \Delta\phi \quad (55)$

Cylinder 2 $I_2 = (-\text{dc term}) -4I_0 J_1(A) \sin \omega_m t \sin \Delta\phi \quad (56)$

(See Figure 10a.)

Taking the difference yields a dc component plus zero differential phase modulation. This zero differential phase modulation will occur if two aluminum drums are wrapped with fiber, the fiber spliced and rotated 90 degrees, and an external phase modulator attached to the system (see Figure 11 for the external phase modulation configuration). Whereas, if PZT cylinder No. 2 was 180 degrees out-of-phase with cylinder No. 1, the results would be a doubled differential phase modulation:

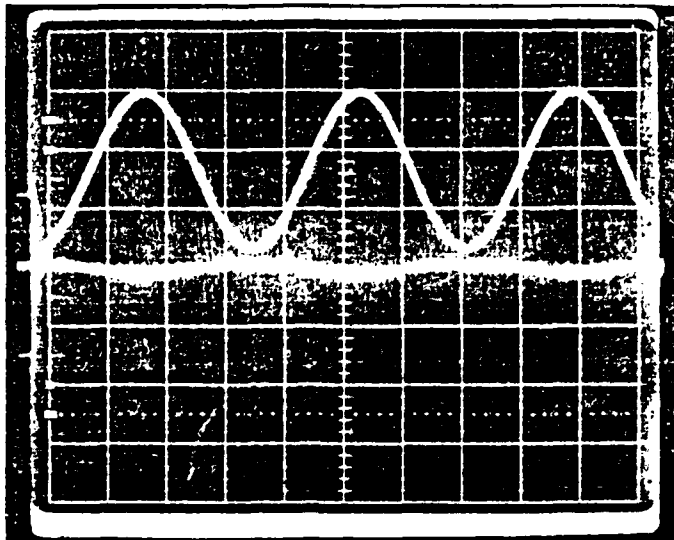
AC modulation

Signal (I)

Cylinder 2 $I_1 = (-\text{dc term}) -4I_0 J_1(A) \sin (\omega_m t - 180 \text{ deg}) \sin \Delta\phi$
 (180 deg
 out-of-phase
 with No. 1) or
 $I_1 = (-\text{dc term}) +4I_0 J_1(A) \sin \omega_m t \sin \Delta\phi \quad (57)$

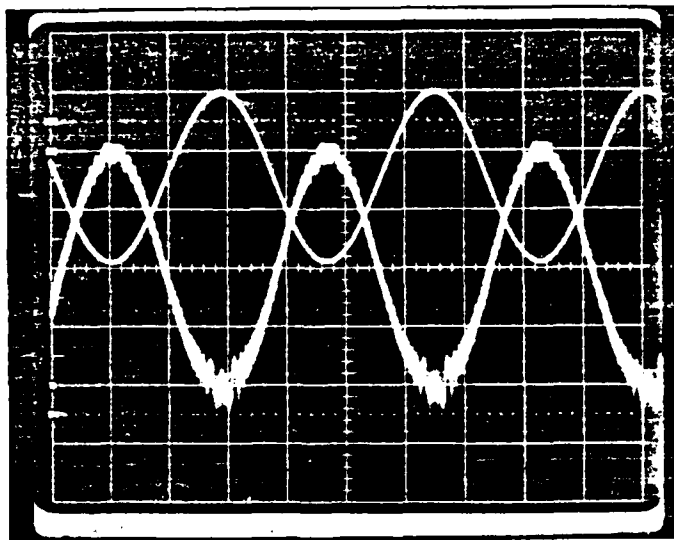
(See Figure 10b.)

Taking the difference of Equations (55) and (57) yields a dc term plus twice the modulation depth and a nonzero differential phase modulation. This approach can be easily implemented by reversing the + and - connections on the second PZT cylinder. Hence, a system utilizing two aluminum drums and an external phase modulator will not work due to zero difference phase modulation.



5mV/DIV = SIGNAL REF = 50 V/DIV SWEEP RATE = .5 msec

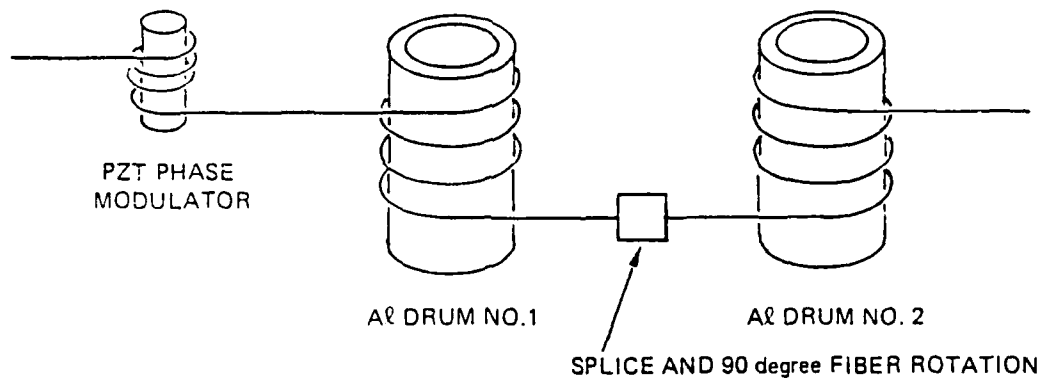
Figure 10a. Two PZT cylinder configuration with fiber rotated 90 deg and spliced. Phase modulation is the same on each cylinder.



10mV/DIV = SIGNAL REF = 50V/DIV SWEEP RATE = .5 msec

TSA 5555

Figure 10b. Two PZT cylinder configuration with fiber rotated 90 deg and spliced. Phase modulation is applied differentially.



TSA 5531

Figure 11. Phase modulation via an external phase modulator.

CHAPTER 4

PRELIMINARY EXPERIMENTAL INVESTIGATION OF THE CSDL FIBER-OPTIC ACCELEROMETER CONCEPT

4.1 Introduction

This chapter will experimentally investigate the type of fiber/cylinder system to be used in the CSDL concept. Polarization, phase, and temperature stability for a single cylinder system, a dual cylinder system, and the CSDL concept will be explored. Differential acceleration sensing via the CSDL concept will be demonstrated and measurements as to the acceleration sensitivity and minimum detectable acceleration made.

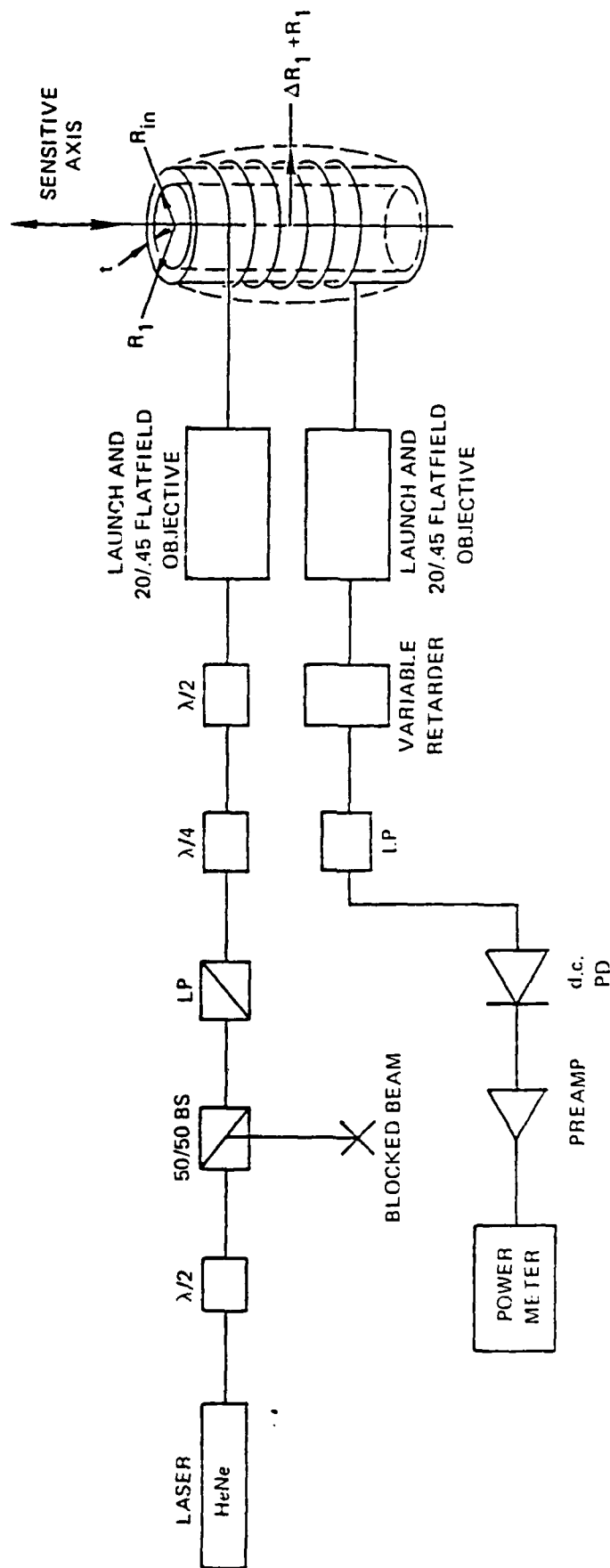
4.2 Tension Coiling a High Birefringent Fiber Around A Cylindrical Drum

An attempt was made to tension coil a small piece of Andrew Corp. elliptical core ($2 \times 1 \mu\text{m}$ core), high birefringent fiber with a $65 \mu\text{m}$ Indium outer jacket and reference flat. Problems identifying and orienting the reference flat during fiber wrapping, along with fiber breakage, made the use of this fiber extremely impractical. Hence, the use of this fiber and the approach of tension coiling a high birefringent fiber was abandoned in favor of tension coiling a York Technology low birefringent fiber or loosely, nontension coiling a York Technology bow-tie high birefringent fiber. No further analysis will be made of the high birefringent fiber tension coiling case.

4.3 Experimental Phase Change Determination of a Single Cylinder Wrapped with Low Birefringent Tension Coiled Fiber

The first experiment consisted of testing a single aluminum cylinder tension coiled with 1 meter of York Technology LB 600 low birefringent fiber, with a $3\mu\text{m}$ core diameter, a $125\mu\text{m}$ cladding diameter, a $210\mu\text{m}$

diameter ultraviolet (UV) cured acrylate jacket, and a 7.8 db/km attenuation at .633 μ m. The aluminum drum had a 6.00 cm O.D. and a 3.2 mm thickness. The drum/fiber parameters were identical to those utilized in determining the system theoretical sensitivity (Section 3.5.1). See Figure 12 for the system configuration. Testing of the system (one drum) involved launching linearly polarized light from a HeNe laser through a $\lambda/2$ plate, a 50/50 beamsplitter, a Glan Thompson Linear Polarizer (GT), a $\lambda/2$ plate, and a 20x/.45 flatfield objective into the optical fiber. It was found that by passing vertical linearly polarized light via $\lambda/2$ plate rotation through the 50/50 beamsplitter, the least light polarization perturbation took place. Only one beam of the 50/50 beamsplitter was used. The other beam was blocked off or used to establish an initial launch into, and an axis orientation of, a later used second fiber wrapped cylinder. The GT linear polarizer was used to extinguish light with unwanted polarization exiting the beamsplitter. The second $\lambda/2$ plate rotated the linearly polarized light by 45 deg prior to launching light into both modes of the fiber. Prior to launching light into the fiber, the light exiting the 20x/.45 objective was analyzed via a $\lambda/4$ plate and an analyzer (GT linear polarizer). It was found that the lens objective had internal birefringence. Consequently, a $\lambda/4$ plate was added prior to the second $\lambda/2$ plate. Combinations of these two optical devices ($\lambda/4$ and $\lambda/2$ plate) yielding linearly polarized light at various orientations was identified. The light at the output end of the fiber was collimated via another 20x/.45 flatfield objective and passed through a variable retarder plate (Babinet Compensator), and a GT linear polarizer prior to hitting a dc photodetector/power meter system with readout in dBs. The variable retarder lined up with the birefringence axis of the fiber serves as a quadrature setting device. The GT linear polarizer rotated 45 degrees relative to the birefringence axis of the fiber serves to optically interfere the two orthogonal polarization modes. Launching linearly polarized light at 45 degrees into the low birefringent fiber involved rotating the $\lambda/4$ plate and second $\lambda/2$ plate until linear polarized light was exiting the fiber (as determined by the $\lambda/4$ plate/analyzer combination). Hence, one of the induced tension



TSA 5556

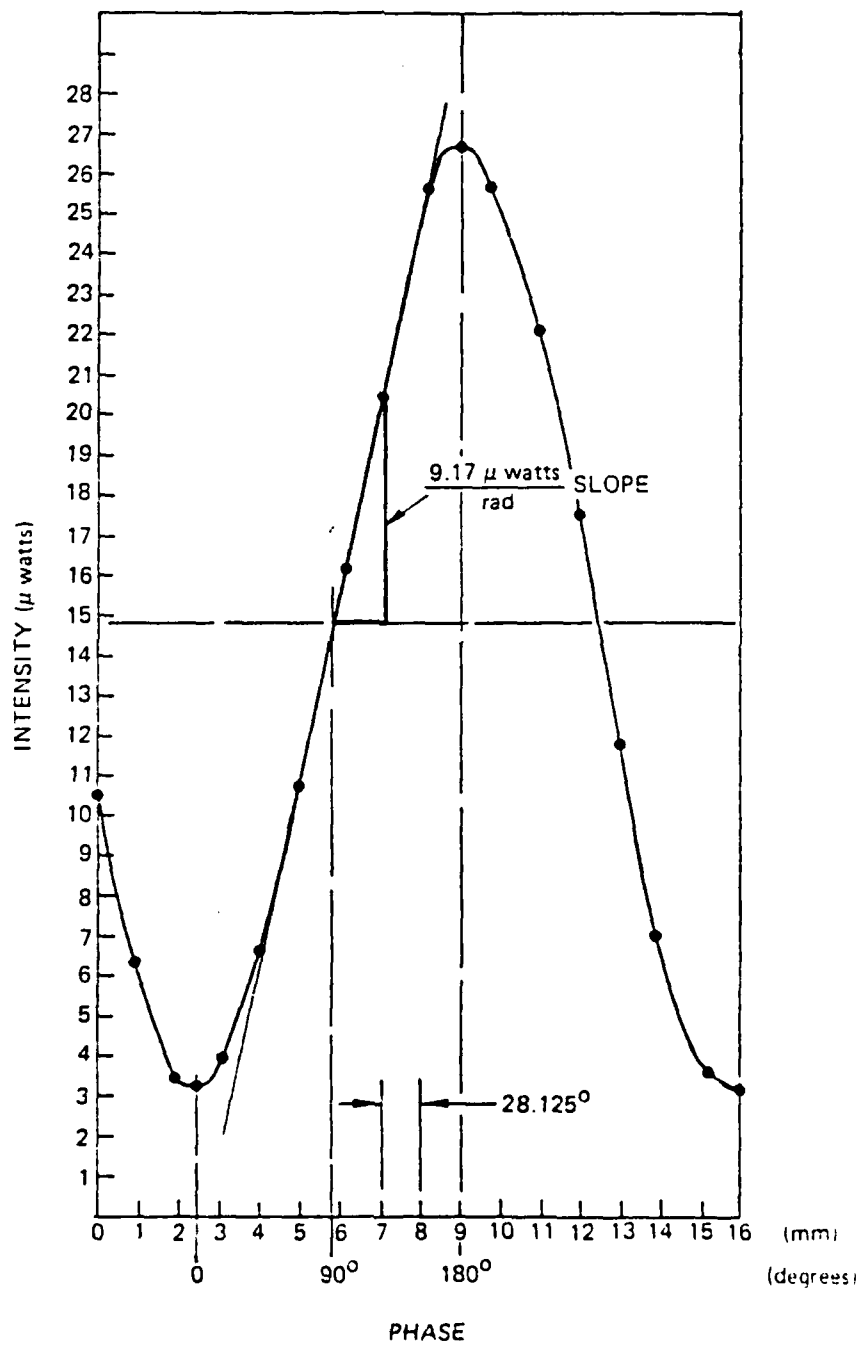
Figure 12. Single cylinder system configuration.

coiling birefringence axis was found. Once the axis was determined, the 45 degree setting of the $\lambda/4$ and $\lambda/2$ plate at the fiber input was easily found and the Babinet Compensator (BC) and GT linear polarizer relative orientation at the fiber output established. A plot of the interference curve was generated by stepping through the BC micrometer positions. The slope (power/rad), was calculated and the BC adjusted for quadrature, i.e., 90 degree phase on the interference curve. A 0.68 kg proof mass was then placed on the aluminum cylinder to simulate induced acceleration. No change in photodetector power output was observed. The minimum resolvable light intensity in dB μ ($\Delta P_{\text{dB}\mu}$) was observed as 0.5 dB μ for the system, as a light percentage

$$\frac{\Delta P}{P} \text{ (in percent)} = 100 \times (1 - 10^{\Delta P_{\text{dB}\mu}/10}) = -12.2\% \quad (58)$$

It is believed that tension wrapping the low birefringent fiber with its acrylate 210 μm outer jacket intact on the fiber resulted in a buffering of the transverse fiber stress. This resulted in only a phase contribution from tension coiling birefringence (-8.43×10^{-4} rad/g). Considering the derived slope of 9.17 $\mu\text{watts/rad}$ from the interference curve (see Figure 13) and the minimum resolvable light intensity, it is clear that no change in power output could have been detected. If, however, the phase change due to transverse fiber stress would have been observed (-1.03 rad/g) with a minimum resolvable light intensity of 0.5 dB μ , a -9.45 μwatt change would have been well observable since at quadrature the light intensity is 39.8 μwatts \times -12.2% minimum resolvable = 4.9 μwatts minimum resolvable. In order to see a -8.43×10^{-4} rad/g phase change, an approximately 1,000 kg mass would have been needed.

In order to allow the β_f mechanism to induce a large phase change in the tension wrapped low birefringent fiber, the fiber would need to be stripped of its outer jacket. A solution of methylene chloride heated was tried to remove the UV cured acrylate outer jacket of the fiber --



TSA 5532

Figure 13. Tension coiled low birefringence/aluminum cylinder interference curve.

this did not strip the jacket off the fiber but caused the fiber ends to swell. Repeated application removed only small segments of the jacket and caused repeated fiber breakage. As a result the tension coiling of low birefringent fiber as a method of inducing orthogonal polarization modes into the fiber was abandoned in favor of the high birefringent nontension coiling approach where stripping of the fiber outer UV cured acrylate jacket was not required. Furthermore, for better cylinder radius change control and eventual adaptation to ac methods the PZT cylinder vs. the aluminum cylinder was utilized for further experimentation and concept verification.

4.4 Experimental Phase Change Determination of a Single PZT Cylinder Wrapped With High Birefringent Nontension Coiled Fiber

A Vernitron PZT-5H cylinder with radial expansion $d_{33} = 5.93 \times 10^{-10}$ m/volt vs. an aluminum cylinder was used. This cylinder was wrapped using light tension, with 3.5 meters of jacketed high birefringence fiber. The fiber used was a York Technology HB 600/2 high birefringent fiber with a 2 mm beat length, a 210 μm UV cured acrylate jacket diameter, a 100 μm cladding diameter, a 4.5 μm core, and an attenuation of 4.0 dB/km at 0.633 μm . The PZT cylinder used had a 5.16 cm O.D. and a 5.52 mm thickness. The system configuration was similar to that in Figure 12. The fiber input and output axis, and the BC and GT linear polarizer orientations were found as previously discussed. Linear polarized light at 45 degrees was launched into the fiber and the PZT was driven incrementally from 0 to 1,000 volts d.c. Data points generating an interference curve slope of (power/volts) = 0.607 $\mu\text{watts/volt}$ and a V_{π} (volts to achieve π radians of phase shift) of 540 volts were taken (see Figure 14). From this a slope in terms of $\mu\text{watts/rad}$ can be calculated to be 104.34 $\mu\text{watts/rad}$. In order to achieve a ΔR_1 equivalent to placing a 0.68 kg proof mass (at 1g) onto the cylinder

$$\Delta R_1 = \frac{\Delta \mu_c R_i \eta}{2\pi R_m E_c t} = (d_{33}) (\text{volts}). \quad (59)$$

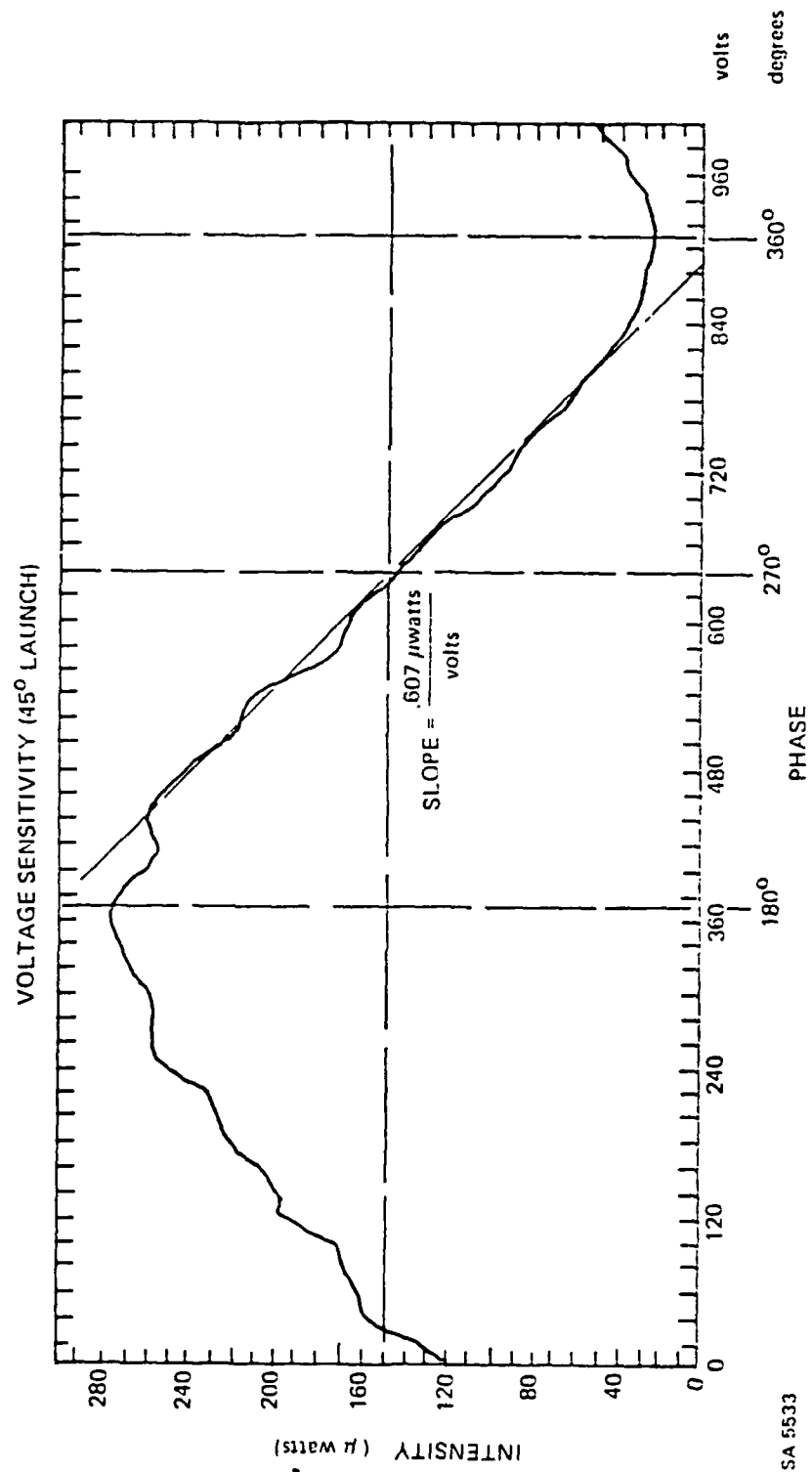


Figure 14. Nontension coiled high birefringence/PZT cylinder case.

Utilizing the appropriate PZT cylinder values we have $\Delta R_1 = 1.17 \times 10^{-9}$ m and 1.97 volts are needed to achieve this ΔR_1 . Corresponding to 1.97 volts a power reading of 1.20 μ watts should result. This was not observed since a minimum resolvable light intensity of 0.5 dB_v (-12.2%) existed; at quadrature (150 μ watts) this would have been equivalent to 18.3 μ watts in order to see a power meter change. Calculating the phase in rad corresponding to 1.97 volts, utilizing $V_{\pi} = 540$ volts, yields 0.70×10^{-2} rad/g which agrees well with the theoretical calculated value of 1.32×10^{-2} rad/g. In order to increase the minimum light intensity detectability, i.e., increase the signal-to-noise ratio thus increasing the minimum light intensity resolution, and simultaneously eliminate low frequency noise as well as electrical noise an ac detection scheme needs to be implemented.

4.5 Polarization, Phase, and Temperature Stability Without Common Mode Rejection

In order to make valid conclusions about accelerometer signal stability due to optical common mode rejection, the two PZT cylinders wrapped with nontension coiled high birefringent fiber must be characterized separately and shown to be identical so that the optical common moding arises from the 90 deg fiber rotation and splicing, and not from inherent system asymmetries acting to dampen any destabilizing effects. Secondly, the CSDL two cylinder fiber-optic accelerometer concept without common mode rejection must be interrogated with results compared to the individual cylinders prior to comparison to the CSDL system with common mode rejection.

4.5.1 Polarization Stability of Each Individual High Birefringent Fiber/PZT Cylinder System

Linearly polarized light was launched into a 2.3 m York Technology high birefringent fiber and rotated via a $\lambda/2$ and $\lambda/4$ plate combination until the orthogonal polarization modes and hence the fiber input and output axes were identified. A Faraday rotator was also added into the

system to reduce any backscatter going into the laser. The high birefringent fiber was symmetrically wrapped around the PZT cylinder with a slight amount of tension and secured via an optical adhesive at two points on the PZT. The fiber was jacketed at all points except for the two fiber ends; one of which was polished at a 10 deg angle (launch end), the other end simply cleaved. The fiber and PZT cylinder parameters were identical to those in section 4.4. To aid in the identification of the fiber orthogonal modes the PZT was driven at a very low frequency (2.5 Hz), and the fiber output analyzed via a GT analyzer set for extinction; minimization of light intensity fluctuation on the dark side determined the location of the fiber axis. The dark and light side intensity fluctuations at the best determinable (within 0.1 deg) mode settings were recorded. At 25.1 dB μ (323.6 μ watts) light intensity input into the fiber, a dark side fluctuation of -17.4 dB μ (1.82×10^{-2} μ watts) to -22.9 dB μ (0.51×10^{-2} μ watts) was observed. This corresponds to a 0.31×10^{-2} μ watt intensity fluctuation at the dark side. At the light side a 13.9 dB μ (24.55 μ watts) reading was obtained with no noticeable intensity fluctuations. Applying the dark side intensity fluctuation to the light side, the intensity fluctuation is only 0.013%. The GT used has a 10^{-5} extinction ratio and the zero light intensity measured was -43.5 dB μ (4.47×10^{-5} μ watts). The fiber extinction ratio was calculated as -34.05 dB μ ($P_{\text{ext}} = P_{\text{dark}} - P_{\text{light}}$), and the subsequent fiber polarization holding parameter h was $4.30 \times 10^{-4}/\text{m}$. The polarization holding parameter is defined as

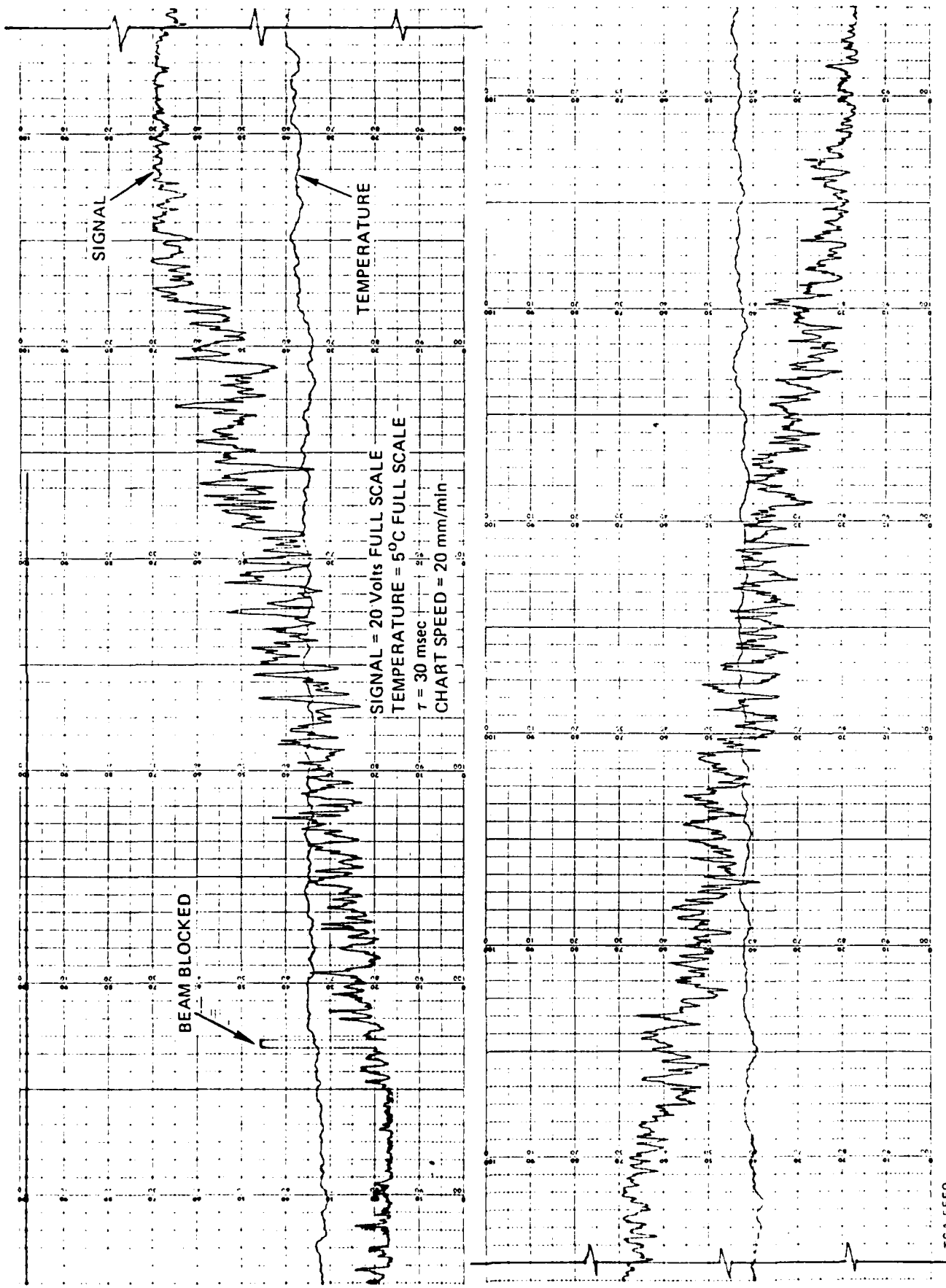
$$h = \tanh^{-1} \left[\log_{10}^{-1} \left(\frac{P_{\text{ext}}}{10} \right) \right] / L \quad (60)$$

where L is the fiber length used. Linear light was beamsplit and launched into an identical second fiber/PZT cylinder. The input and output axis were found as before. The dark side intensity fluctuation was recorded at 2.08×10^{-2} μ watts. Applying this dark side intensity fluctuation to the light side yielded a 0.27% light intensity

fluctuation. The extinction ratio and the polarization holding parameter for the second fiber/PZT cylinder were -29.45 dB_μ and $4.94 \times 10/\text{m}^{-4}$ respectively. To verify that light was launched into one of the polarization modes of the high birefringent fiber the PZT driving voltage was turned off and a thermal impulse was induced into the fiber by touching the fiber coil on the PZT cylinder. For both coils the light intensity fluctuations did not change from the previous readings. These values compared well with those of the first fiber/PZT cylinder. The h factors of the two separate fiber/PZT cylinders were an order of magnitude greater than expected. This is attributable to the roughness of the PZT cylinder surface, and the propagation of cladding modes.

4.5.2 Phase and Temperature Stability of Each Individual High Birefringent Fiber/PZT Cylinder System

Once the input and output axes of each fiber were identified light was easily launched at 45 deg into both modes of the fiber. A BC with axis parallel to that of the fiber output axis and a GT analyzer set at 45 deg relative to the fiber output axis for quadrature control and polarization mode interference was added. Furthermore, in order to increase the minimum detectable light intensity, the propagating light was phase modulated by driving the PZT at a frequency of less than 1 kHz and 300 volts p-p via a Wavetech signal generator and a high voltage amplifier. The dc photodetector and power meter were replaced with an ac coupled photodetector with a dc to 10 MHz bandwidth. The ac photodetector signal was then demodulated via a lock-in amplifier, referenced to the PZT driving frequency, and the lock-in output recorded on a strip chart recorder. A temperature probe was inserted into the single PZT cylinder and the temperature was recorded along with the signal on the strip chart recorder (see Figure 15). Both fiber/PZT cylinders were tested in the same manner and the outputs compared. In both cases the temperature drift was $180 \text{ deg phase}/.35^\circ\text{C}$ and the max rms phase fluctuation at quadrature with a lock-in time constant of 30 msec was $1.18 \times 10^{-2} \text{ rad}$. It is clear Figure 15 represents the typical



TSA 5559

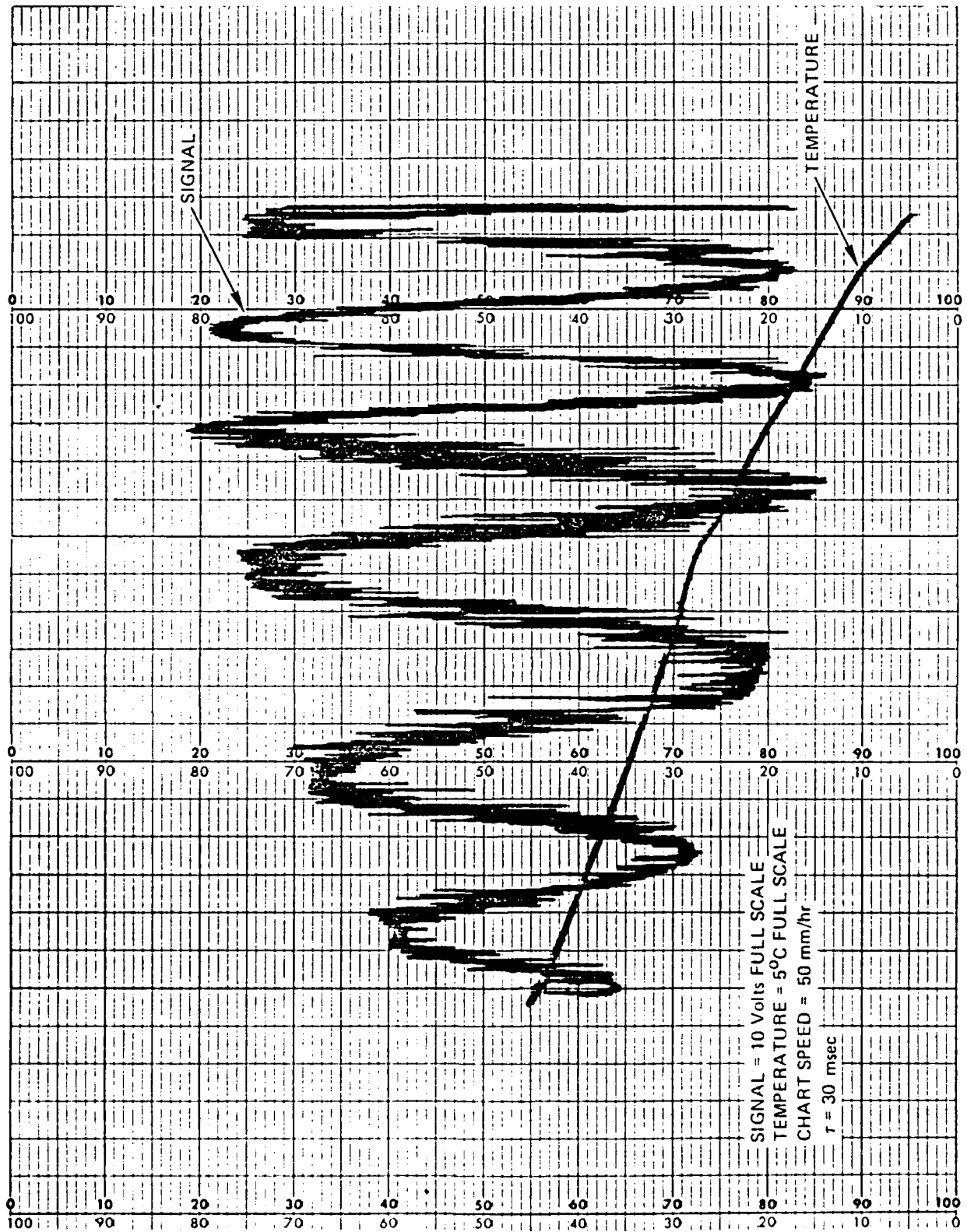
Figure 15. Single cylinder thermal and phase stability data.

thermal and phase stability of a nonisolated high birefringent nontension wrapped PZT cylinder utilizing phase modulation for this system.

4.5.3 Polarization, Phase, and Temperature Stability of the Two Cylinder High Birefringent System

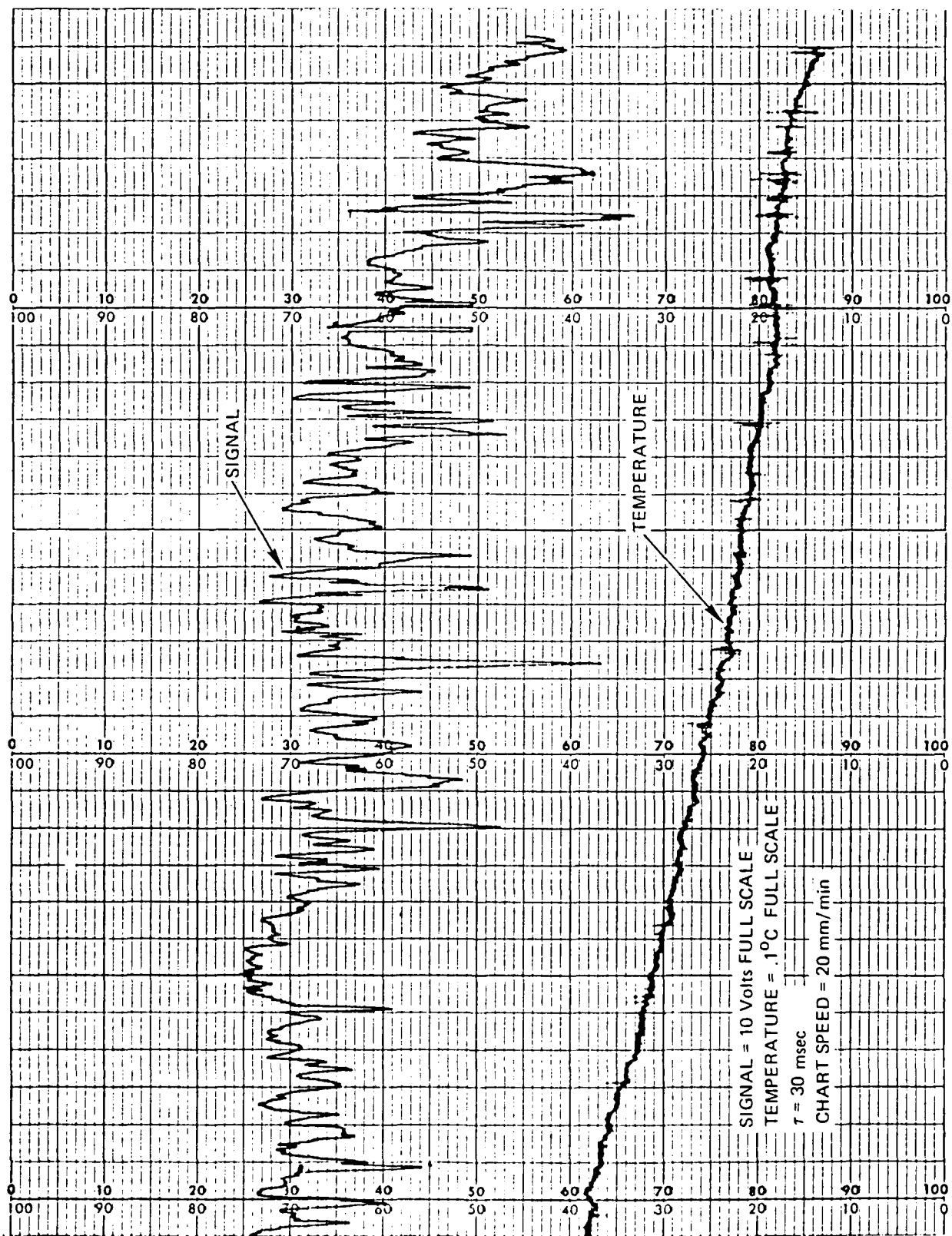
To determine what the polarization, phase and temperature stability of the two drums without common mode rejection is, the two cleaved ends both secured in pencil vises and 0.1 degree rotators, one from each fiber, were butt coupled using 0.5 μm micropositioners, with the fast axis of one aligned with the fast axis of the other and similarly for the slow axis. An index matching oil was capillaried into the fiber-to-fiber gap to minimize fiber light scattering. The two cylinders were brought as close together as possible without causing any shorting (approximately 2 cm), isolated from the environment (air currents, thermal gradients etc.), and driven nondifferentially at 2.5 Hz and 300 volts p-p. Light was launched into one mode and the light and dark side fluctuations notated as 4.4×10^{-1} and 9.2×10^{-2} μwatts (7.13%), respectively. The extinction ratio was -21.30 dB_u and the polarization holding parameter was $1.61 \times 10^{-3}/\text{m}$.

Linear light was now launched at 45 deg into the fiber, the PZT's driven nondifferentially at less than 1 kHz and 300 volts p-p, signal and temperature recorded similarly to what was done in section 4.5.2. The average temperature drift was 180 deg phase/.35°C as shown in Figure 16. This was very close to the nonenvironmentally isolated single cylinders tested. If the dual PZT cylinder configuration was not environmentally isolated, a much worse temperature drift than the individual cylinder case would have been observed. The fluctuation of the p-p photodetector interference curve is attributed to an intensity fluctuation resulting from fiber-to-fiber butt joint movement due to vibration and thermal gradients. At quadrature the photodetector scale was opened up and the phase stability observed as shown in Figure 17. The max rms phase fluctuation at quadrature with a lock-in time constant of 30 msec was 2.00×10^{-2} rad.



TSA 5561

Figure 16. Two cylinder thermal and phase stability data.



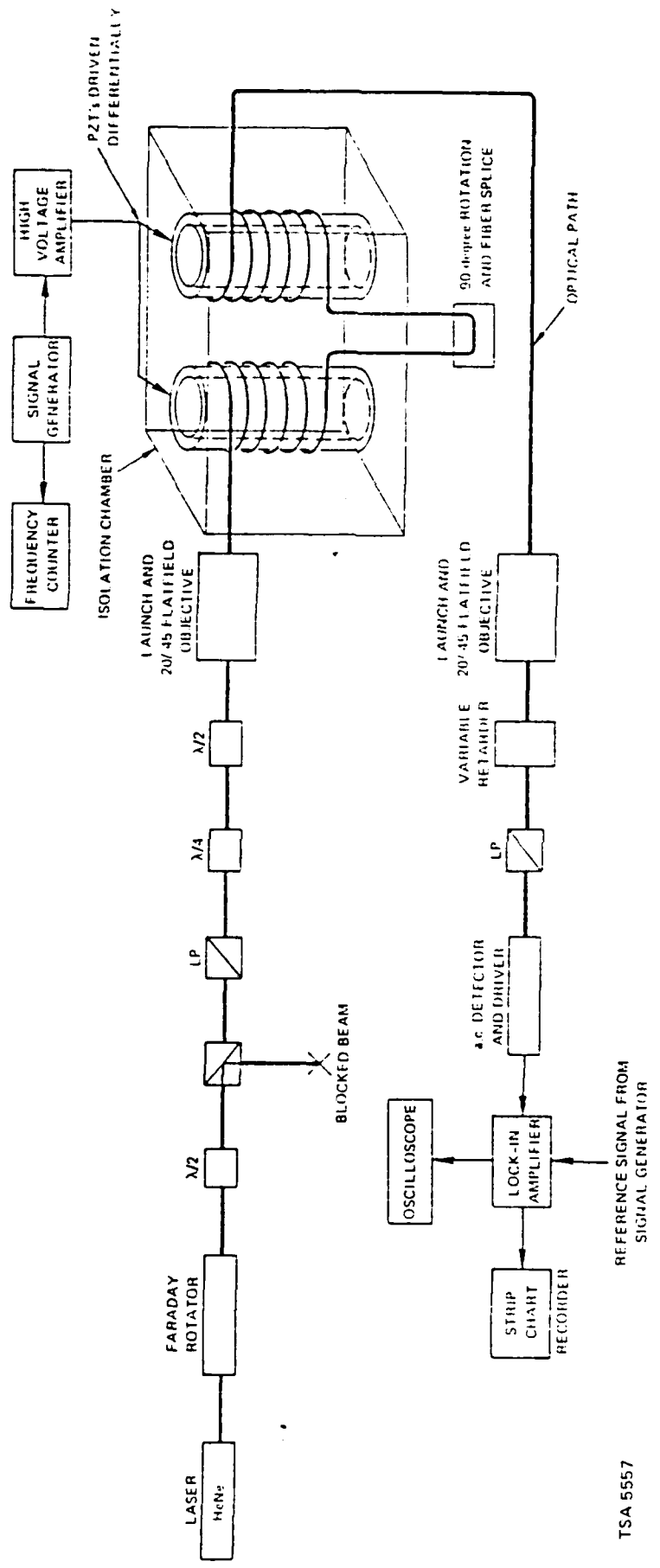
TSA 5562

Figure 17. Signal at quadrature for the two cylinder system.

4.6 Polarization, Phase, and Temperature Stability With Common Mode Rejection

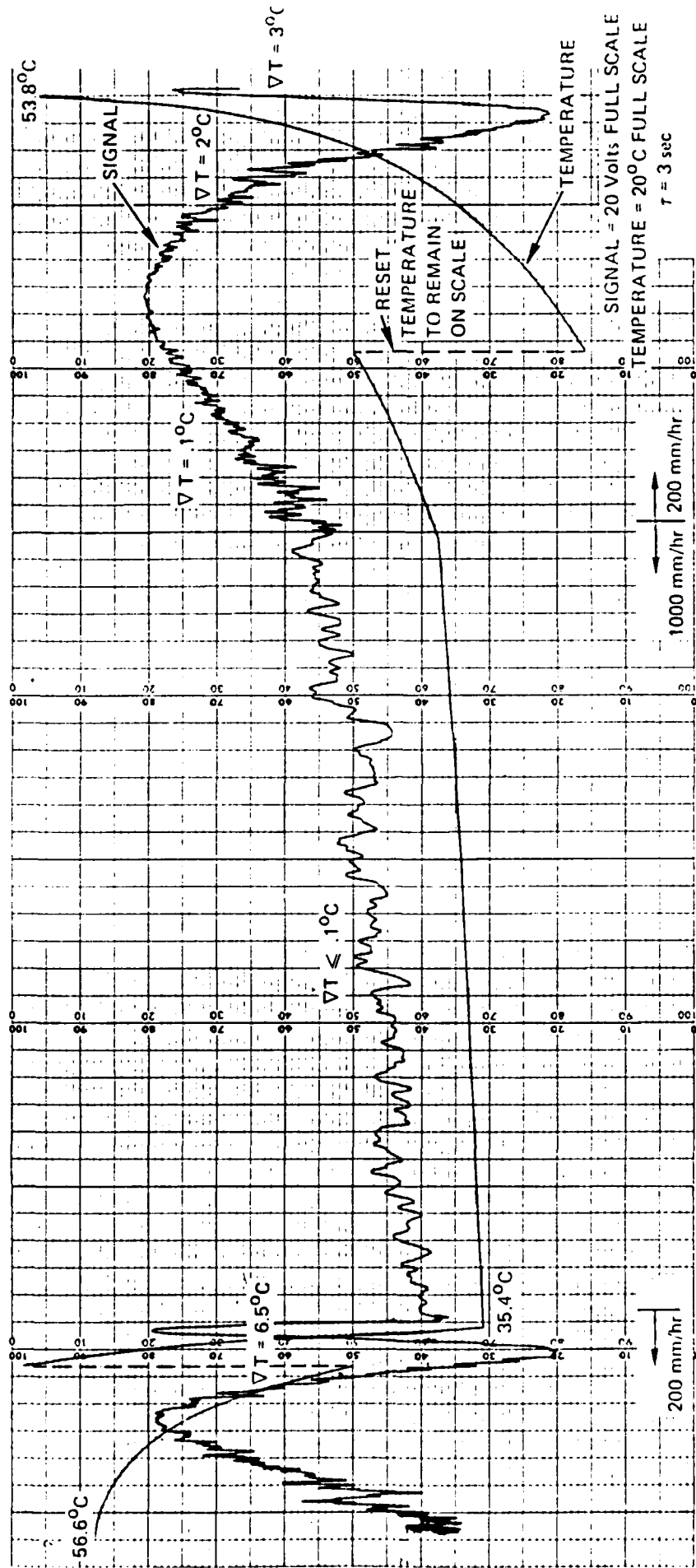
One of the cleaved fiber ends was now rotated 90 deg and spliced to the second fiber for optical common moding. Fiber rotation was accomplished by rotating the pencil vise holding the cleaved fiber. A splice was performed utilizing UV curable optical adhesive. Splice rigidity was achieved by using a thin piece of glass (0.1 mm thickness) for support. To eliminate any cladding mode light propagation, mode strippers at the input end of each fiber were used. The two fiber/PZT cylinders were still environmentally isolated and the PZT's were driven differentially (see Figure 18 for the system configuration). The polarization stability was determined as before; the dark side intensity fluctuation was 7.01×10^{-2} μ watts, while no light side intensity fluctuation was observed. Applying the dark side light fluctuation to the light side yielded a 0.61% light intensity fluctuation. The extinction ratio was -17.6 dBu and the polarization holding parameter was $3.82 \times 10^{-3}/m$.

In order to measure the temperature stability of the system the isolated environment of the two cylinders was heated. Light was launched at 45 deg into the fiber and the temperature was raised 20°C and allowed to return to ambient. Two temperature probes, one in each cylinder, monitored the temperature while the system was allowed to run. The photodetector/lock-in signal and one cylinder temperature was recorded via a strip chart recorder while the second cylinder temperature was monitored. The thermal drift measured corresponded to 180 deg phase/7.5°C. Large thermal gradients ($\nabla T = 3.0^\circ C$) between the two cylinders were observed during the steepest temperature drop, (first 180 deg phase shift), with thermal gradients becoming less than 0.1°C towards ambient temperature. At this point the photodetector signal scale was opened up and the rms phase stability with a 3 sec lock-in time constant was observed as 6.66×10^{-3} rad (see Figure 19 for strip



TSA 5557

Figure 18. Two cylinder system with common mode rejection configuration.



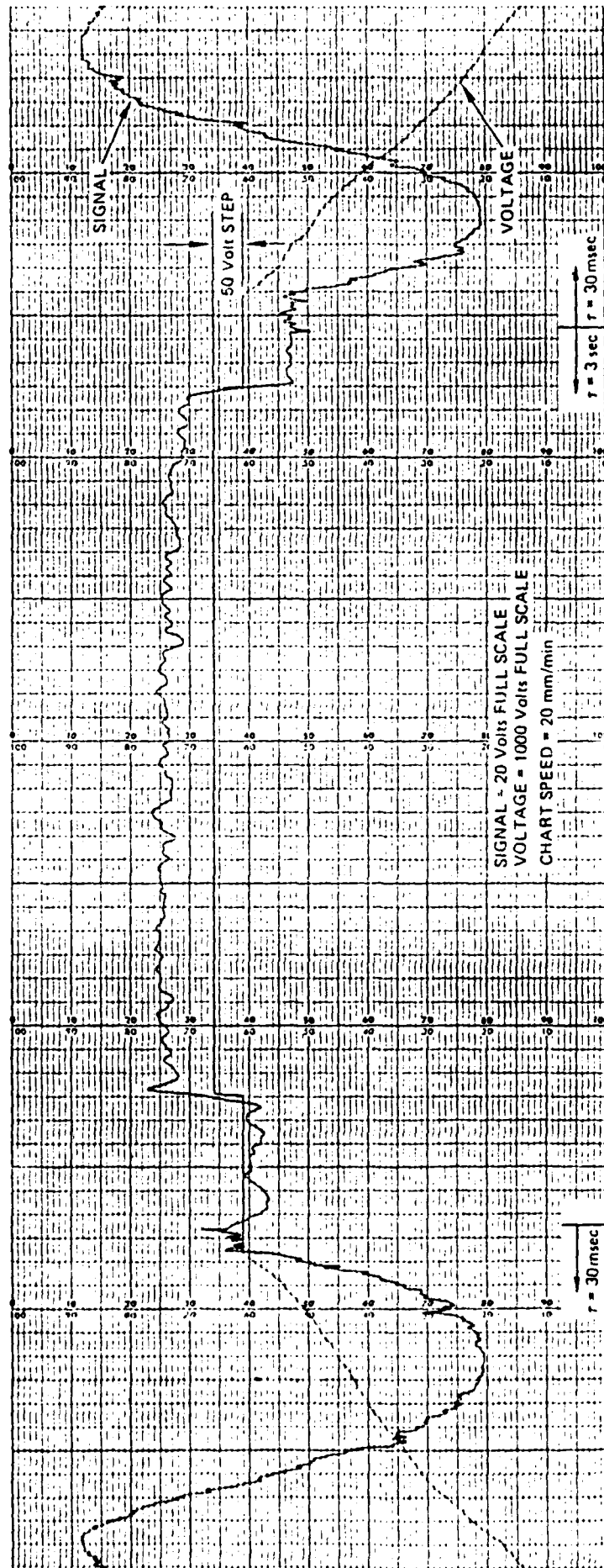
TSA 5560

Figure 19. Common mode rejection thermal drift data.

chart data). A 3 sec time constant was used to reduce the effects of table vibration and overall optical component mechanical vibration. Using a 30 msec time constant the max rms phase stability at quadrature was 1.11×10^{-2} rad.

4.7 Experimental Demonstration of Acceleration Sensing

The system was configured for optical common mode rejection as before and a dc voltage of 100 to 610 volts was applied differentially to the two fiber wrapped, isolated PZT cylinders in order to drive the system through 360 deg phase shift. V_{π} was measured to be 300 volts. The temperature was closely monitored to insure that thermal gradients were less than 0.1°C. A 50 volt dc step input was induced differentially into the system and the response determined. Using the measured signal voltage change for a 50 volt step input, V_{π} for the system, and the theoretical scale factor $\frac{\Delta\phi}{\Delta\alpha}$ of -1.73×10^{-2} rad/g derived from equation (47) using a 2.3 m fiber length, the system phase change was 2.16 deg and the measured acceleration was 2.18 g's. The measured minimum detectable rms phase shift ($\Delta\phi_{\min \text{ det}}$) was 2.22×10^{-3} rad. This yields a minimum detectable acceleration ($\Delta\alpha_{\min \text{ det}}$) of 0.13 g's (see Figure 20 for measured values). The CSDL fiber-optic accelerometer testbed was not readily vertically rotatable and hence could not be easily tested on a 0 to 1 g rotatable head for actual scale factor and bias determination.



TSA 5563

Figure 20. Common mode rejection V_{π} and induced acceleration data.

CHAPTER 5

EXPERIMENTAL DISCUSSION OF RESULTS

Initial experimentation with 1) tension coiling, reference flat, high birefringent Andrew Corp. fiber; 2) tension coiling low birefringent York fiber; and 3) loosely wrapping York high birefringent fiber, indicated that severe handling problems existed with 1 and 2. Consequently, choice 3 was adopted and investigated. The differential phase modulation required to reduce electrical and $1/f$ noise, and increase the minimum resolvable light intensity for differential sensing of dc acceleration, dictated that PZT cylinders be used. Once it was determined that a PZT cylinder was needed to provide differential phase modulation, actual PZT cylinder dimensional changes would act negligibly on the system sensitivity. It is however desirable to increase the fiber length by an order of magnitude and decrease the proof mass by more than an order of magnitude. A long fiber length will propagate fewer cladding modes and hence will be easier to determine the fiber axis.

Linear light $\lambda/2$ rotation to within 0.1 deg was required in order to achieve a 10^{-4} m polarization holding parameter. Polarization stability in both high birefringent fiber/PZT cylinders was identically around $10^{-4}/m$, indicating congruence. This h factor was, however, an order of magnitude larger than expected and is postulated to have occurred due to cylinder surface roughness and cladding mode propagation in the 2.3 meter fiber length. Fiber multi-mode characteristics also need to be investigated. Comparing the single cylinder with the dual cylinder, both with and without common mode rejection, we see an order of magnitude increase in h factor for the dual cylinder case. This is attributable to a not exact 90 deg fiber rotation. It is estimated that the 90 deg fiber rotation alignment could be off as much as 5 deg. A more reliable 90 deg fiber rotation will need to be utilized in order to align the fibers within 0.1 deg prior to splicing. However, comparing

the noncommon moded with the common moded system polarization stability we see a decrease in light side intensity fluctuations from 7.13% to 0.61% by going to common mode rejection.

The phase stability of the two separate high birefringent fiber/PZT cylinders, as well as the phase stability of the common moded and noncommon moded cases, was similar at 10^{-2} rad. This indicates that at the common mode rejection level achieved, signal noise was not reduced. However, at 10^{-4} common mode rejection, signal noise should be significantly reduced. A further conclusion is that splicing the rotated fiber ends with UV curable adhesive did not eliminate any phase noise but reduced the intensity drift.

Thermal stability of each high birefringent fiber/PZT cylinder was 180 deg phase shift/.35°C. Each cylinder was, however, not isolated in a closed chamber and thus affected by air fluctuations and thermal gradients. The dual cylinder noncommon mode rejection system also exhibited 180 deg phase shift/.35°C; however, both drums were fully isolated from the environment. Optical common mode rejection improved the thermal drift characteristics of the fiber-optic accelerometer system; 180 deg phase shift/7.5°C. This is a 21 fold improvement over the noncommon mode rejection case. Theoretically a 4 order of magnitude improvement due to optical common moding should have been observed²⁰. Nonexact 90 deg fiber rotation and thermal gradients are the limiting factors for not achieving theoretical optical common mode rejection. To eliminate thermal gradients the two fiber/cylinder configuration would involve stacking one cylinder on top of another and isolating them from the environment.

Sensing of acceleration in thermal gradients of less than 0.1°C indicated a minimum detectable rms phase of 2.22×10^{-3} rad and a minimum detectable rms acceleration of 0.13 g's. Using ± 45 deg as the maximum operating point at which the scale factor is still linear, the rms maximum detectable acceleration is 1.94 g's. This yields a dynamic range of 15. However once a minimum detectable rms phase of 1 μ rad is achieved the dynamic range becomes 10^4 .

The theoretical limit on phase shift shot noise detection can be calculated via²¹

$$\delta(\Delta\phi) = \frac{\pi}{\sqrt{n_{ph} n_D \tau}} = 3.70 \times 10^{-7} \text{ rms} \quad (61)$$

where

n_D is the photodetector/amplifier efficiency = .60
 τ is the lock-in amplifier time constant = 3 sec
 n_{ph} is the number of photons/sec falling on the detector and following a Poisson distribution.

$$n_{ph} = \frac{P}{h\nu} = 4.0 \times 10^{13} \text{ photons/sec} \quad (62)$$

where

P is the detector incident power = 12.5 watts
 h is Planck's constant = 6.6×10^{-34} J s
 ν is the HeNe frequency = 4.74×10^{14} Hz.

Comparing the experimental minimum detectable rms phase shift of 2.22×10^{-3} rad to the theoretical shot noise limited detection of 3.70×10^{-7} rad, a 4 order of magnitude discrepancy exists. The prevalent noise source is clearly phase noise, and not amplitude noise, arising from physical environmental perturbations such as acoustic noise and component mechanical vibration. These can be eliminated by pinning down all loose fiber, and bringing the splice into the isolation chamber and closer to the two cylinders. Other acoustical noise can be eliminated by enclosing the entire system in a plexiglass chamber with the electronics outside the chamber. Second order phase noise to be eliminated would be any polarization modulation due to asymmetric light

launching into an angle polished vibrating fiber by stabilizing the fiber. Additional second order phase instability is attributable to the effective thermal expansion coefficient of the fiber jacket and the silica core. This effective expansion coefficient is approximately 15 ppm/°F or roughly that of aluminum²². Furthermore, detector/amplifier noise could not have been a limiting factor since the detector had an rms noise level of 20×10^{-12} rad/ $\sqrt{\text{Hz}}$.

CHAPTER 6

SUMMARY, CONCLUSIONS, AND RECOMMENDATIONS

6.1 Summary and Conclusions

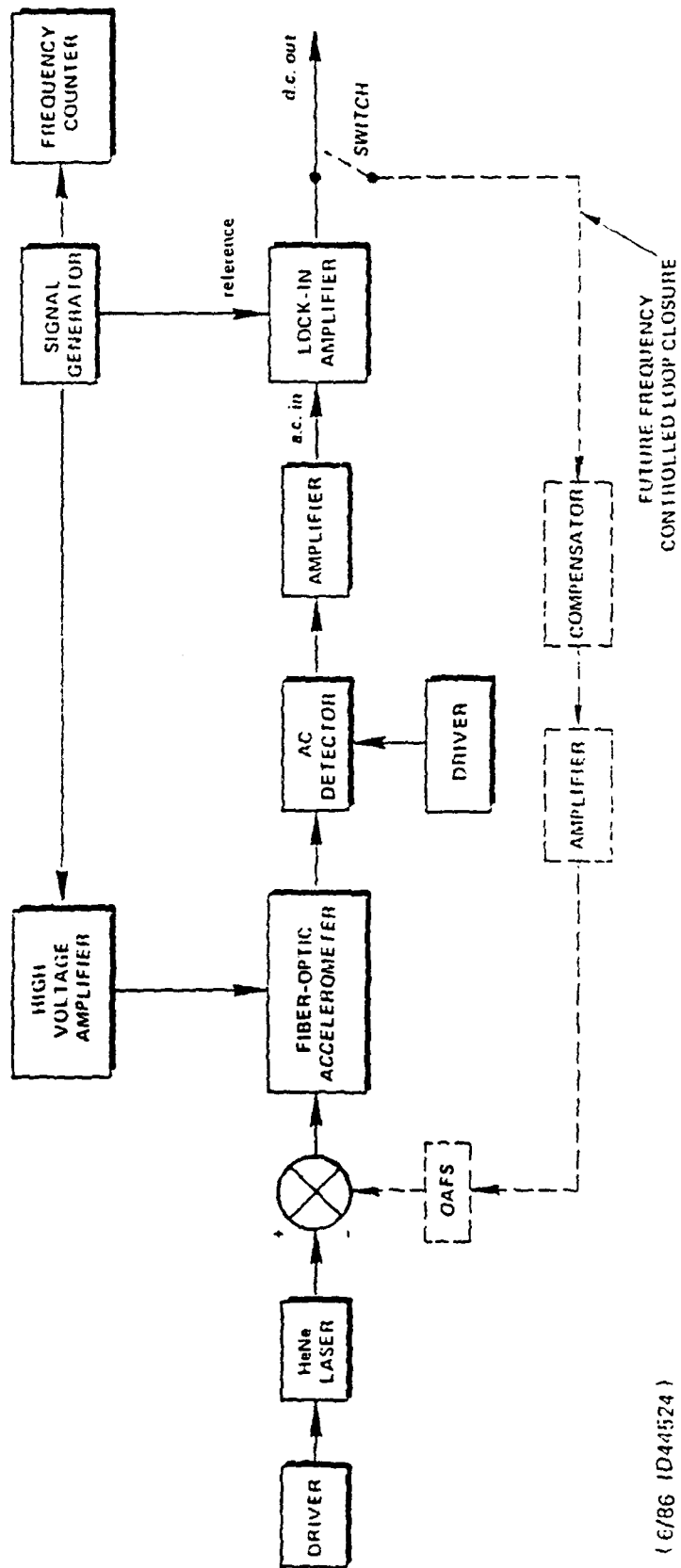
Several fiber-optic accelerometer concepts have been reviewed. From these concepts a fiber-optic accelerometer concept utilizing optical common mode rejection in a two cylinder single mode fiber wrapped system emerged. This concept was experimentally investigated in a preliminary way. Initial experimentation indicated that the use of low birefringent and reference flat high birefringent fiber was undesirable. Regular bow tie, high birefringent fiber, loosely wrapped without regards to internal axis orientation, became the fiber choice and method of application. The calculated scale factor $\frac{\Delta\phi}{\Delta a}$ was -1.73×10^{-2} rad/g at 0.68 kg and 2.3 meters of fiber on each cylinder, and the system bias was -3.83 rad, primarily due to nonzero fiber birefringence. The measured phase shift agreed well with calculated results and literature predicted phase shift sensitivities. Differential phase modulation required to increase the minimum detectable light intensity governed the use of PIT cylinders for sensor use and provided an ideal setup for interrogating the concept. Both cylinders were characterized separately and compared to the dual cylinder common mode and noncommon mode operation. Polarization stability defined by the polarization holding parameter decreased from $10^{-4}/m$ for the individual cylinders to $10^{-3}/m$ for the dual cylinder common mode rejection case. Optical common mode rejection via a 90 deg fiber rotation and splice reduced thermal drift 21 fold. However, no effect on phase stability was noted. Phase stability remained at 10^{-2} rad. Splicing the fiber with UV curable adhesive reduced intensity drift. The dc acceleration sensed due to a 50 volt dc differential input was 2.18 g's. Using a 3 sec lock-in time constant the system displayed a $\Delta\phi_{\min \text{ det}}$ of 10^{-3} rad. Overall system dynamic range was poor but promises to be at 10^4 when a $\Delta\phi_{\min \text{ det}}$ of 1 μ rad is achieved.

The dominant noise is phase noise and is primarily attributable to lousy environmental conditions and nonrigid hardware mounting. Shot noise limited phase detection is at 10^{-7} rad; this is a factor of 4 from what was measured. Improving environmental conditions, stabilizing the optics, reducing cleaved fiber end backscatter at the splice, and achieving a better than 0.1 deg fiber rotation will bring down the signal noise level to within shot noise performance.

6.2 Recommendations

The CSDL fiber-optic accelerometer concept has good potential for becoming a viable instrument. However, the mechanical vibrations in the system must be reduced and the signal phase noise level reduced to within shot noise performance. To achieve the former, system optical components must be brought closer to the working surface of the floating table, the common mode rejection splice must be decoupled from the micropositioners/rotators and brought closer to the PZT cylinders, and the fiber/PZT cylinders isolated from acoustic perturbations. To achieve a phase noise reduction a longer fiber length (approximately 20 meters on each drum), should be used and the fiber mode stripped to eliminate cladding mode propagation. The fiber multi-mode behavior should also be experimentally investigated. Further system optical common mode rejection improvement could be achieved by more precise 90 deg fiber rotation; for example, with the use of a Pockels cell where minimum polarization modulation would identify the orthogonal polarization axis of the high birefringent fiber. To realize the improvement of precise 90 deg fiber rotation and common mode rejection at the 10^{-4} theoretical limit for thermal drift, the two PZT cylinders need to be grounded thermally by placing one cylinder on top of the other with a proof mass in between, without electrically shorting the PZT's. Hence, thermal gradients will be eliminated and thermal drift further reduced. Lastly, in order to achieve an instrument configuration and keep the system at quadrature, closed loop operation needs to be implemented. This could be accomplished, for example, by frequency controlled loop closure as illustrated in Figure 21. Here the

lock-in amplifier dc signal goes through a lead/lag compensator prior to being amplified and frequency shifted by an acousto-optic frequency shifter (AOFS). The frequency shift required to null the system measures the induced acceleration. Furthermore, the proof mass utilized in the system should also be reduced to less than 500 grams if an instrument configuration is to be realized.



(6/86 1044324)

TSA 5558

Figure 21. Frequency controlled loop closure.

REFERENCES

1. Dr. Marc S. Weinberg, CSDL, Cambridge, MA., private communications, November, 1985.
2. William C. Albert and Raymond E. Weber, "Vibrating Beam Accelerometer for Strapdown Applications", Singer Company, Kearfott Div., Fairfield, NJ.
3. William C. Albert, "Vibrating Quartz Crystal Beam Accelerometer", ISA 28th International Instrumentation Symposium, Vol. 28, No. 1, 1982, pp. 33-44.
4. A. D. Kersey, D. A. Jackson and M. Corke, "High-Sensitivity Fibre-Optic Accelerometer", Electronics Letters, Vol. 18, No. 13, 24 Jun 82.
5. Shuichi Tai, Kazuo Kyuma, Masahiro Nunoshita, "Fiber-Optic Acceleration Sensor Based on the Photoelastic Effect", Applied Optics, Vol. 22, No. 11, 1 June 83.
6. Richard A. Soref and Donald H. McMahan, "Tilting-Mirror Fiber-Optic Accelerometer", Applied Optics, Vol. 23, No. 3, 1 Feb 84.
7. Frank L. Stokes, "Single-Mode Optical Fiber Resonator and Applications to Sensing", Thesis Ginzten Lab Report #3620, Stanford University, Sept. 83.
8. Scott C. Rashleigh, "Origins and Control of Polarization Effects in Single-Mode Fibers, Journal of Lightwave Technology, Vol. LT-1, No. 2, June 83.
9. S. C. Rashleigh, "Magnetic-field Sensing with a Single-mode Fiber," Optics Letters, Vol. 6, No. 1, January 1981.

10. Scott C. Rashleigh, "Polarimetric Sensors: Exploiting the Axial Stress in High Birefringent Fibers", in Proc. First IEE Dit. Conf. Optical Fiber Sensors (London, U.K.), Apr. 1983, pp. 210-212.
11. R. Ulrich, S.C. Rashleigh, and W. Eickhoff, "Bending-Induced Birefringence in a Single-Mode Fiber", Optics Letters, Vol. 5, No. 6, June 80.
12. D. E. Gray, Ed., American Institute of Physics Handbook, 3rd Ed., (McGraw-Hill, New York, 1972).
13. Scott C. Rashleigh and R. Ulrich, "High Birefringence in Tension-Coiled Single-Mode Fibers", Optical Letters, Vol. 5, No. 8, August 1980.
14. S. R. Rengarajan and J.E. Lewis, "First Higher-mode Cutoff in Two-layer Elliptical Waveguides," Electronics Letters, Vol. 16, pp 263-264, 1980.
15. Malcolm P. Varnham, David N. Payne, Arthur J. Barlan, and Robin N. Birch, "Analytic Solutions for the Birefringence Produced by Thermal Stress in Polarization-Maintaining Optical Fibers," Journal of Lightwave Technology, Vol. LT-1, No. 2, June 1983.
16. Malcolm P. Varnham, David N. Payne, Arthur J. Barlan, and Robin N. Birch, "Polarimeter Strain Gauges Using High Birefringent Fiber," Electronic Letters, Vol. 19, No. 17, August 1983.
17. Timoshenko, SP, and F.N. Goodier, Theory of Elasticity, McGraw-Hill, New York, 1934.
18. Roark, Raymond J. and Warren C. Young, Formulas for Stress and Strains, 5th Edition, McGraw-Hill, Inc., New York, 1975.

19. McMahon, G.W. and P.G. Cielo, "Fiberoptic Hydrophone Sensitivity for Different Sensor Configurations," *Applied Optics*, Vol. 18, No. 22, pp 3720-3722, 15 November 1979.
20. Dr. Raymond Carroll, CSDL, Cambridge, MA, Private Communications, September 1986.
21. S. Ezekiel and H.J. Arditty, Fiber-optic Rotation Sensors and Related Technologies, Vol. 32, (New York 1982), published proceedings of the 1st International Conference on Fiber-optic Rotation Sensors, MIT, Cambridge, MA, Nov 9-11, 1981.
22. F. Petri, "Fiber-optic Thermal Strain Analysis," CSDL Memo 30H-85-180, Charles Stark Draper Laboratory, Cambridge, MA, Dec 28, 1985.

END

11-87

DTIC